

Alma Mater Studiorum Università di Bologna
Archivio istituzionale della ricerca

High-pressure serpentinization and abiotic methane formation in metaperidotite from the Appalachian subduction, northern Vermont

This is the final peer-reviewed author's accepted manuscript (postprint) of the following publication:

Published Version:

Boutier, A., Vitale Brovarone, A., Martinez, I., Sissmann, O., Mana, S. (2021). High-pressure serpentinization and abiotic methane formation in metaperidotite from the Appalachian subduction, northern Vermont. LITHOS, 396-397, 1-17 [10.1016/j.lithos.2021.106190].

Availability:

This version is available at: <https://hdl.handle.net/11585/827262> since: 2021-07-02

Published:

DOI: <http://doi.org/10.1016/j.lithos.2021.106190>

Terms of use:

Some rights reserved. The terms and conditions for the reuse of this version of the manuscript are specified in the publishing policy. For all terms of use and more information see the publisher's website.

This item was downloaded from IRIS Università di Bologna (<https://cris.unibo.it/>).
When citing, please refer to the published version.

(Article begins on next page)

This is the final peer-reviewed accepted manuscript of:

Boutier, A.; Vitale Brovarone, A.; Martinez, I.; Sissmann, O.; Mana, S.: *High-pressure serpentinization and abiotic methane formation in metaperidotite from the Appalachian subduction, northern Vermont*

LITHOS. VOL. 396-397. ISSN 0024-4937

DOI: 10.1016/j.lithos.2021.106190

The final published version is available online at:

<https://dx.doi.org/10.1016/j.lithos.2021.106190>

Terms of use:

Some rights reserved. The terms and conditions for the reuse of this version of the manuscript are specified in the publishing policy. For all terms of use and more information see the publisher's website.

This item was downloaded from IRIS Università di Bologna (<https://cris.unibo.it/>)

When citing, please refer to the published version.

**High-pressure serpentinization and abiotic methanogenesis in metaperidotite from the
Appalachian subduction, northern Vermont**

Antoine Boutier^{1,2*}, Alberto Vitale Brovarone^{1,3,4}, Isabelle Martinez², Olivier Sissmann⁵, Sara
Mana⁶

¹*Dipartimento di Scienze della Terra, Università degli Studi di Torino, Via Valperga Caluso 35,
Torino, Italy*

²*Université de Paris, Institut de physique du globe de Paris, CNRS, F-75005 Paris, France*

³*Dipartimento di Scienze Biologiche, Geologiche e Ambientali, Alma Mater Studiorum
Università di Bologna. Piazza di Porta San Donato 1, Bologna, Italy*

⁴*Institut de Minéralogie, de Physique des Matériaux et de Cosmochimie (IMPMC), Sorbonne
Université, Muséum National d'Histoire Naturelle, UMR CNRS 7590, IRD UR206, 75005 Paris,
France*

⁵*IFP Energies Nouvelles, 92500 Rueil-Malmaison, France*

⁶*Department of Geological Sciences, Salem State University, Salem, MA 01970, USA*

*Corresponding author: antoine.boutier@unito.it

1 **Abstract**

2 Serpentinization is the process of hydroxylation of olivine-rich ultramafic rocks to produce
3 minerals such as serpentine, brucite and magnetite. This process is commonly accompanied
4 by Fe oxidation and release of H₂, which can be involved in abiotic reaction pathways leading
5 to the genesis of abiotic light hydrocarbons such as methane (CH₄). Examples of this
6 phenomenon exist at the seafloor, such as at the serpentinite-hosted Lost City hydrothermal
7 field, and on land in ophiolites at relatively shallow depths. However, the possibility for
8 serpentinization to occur at greater depths, especially in subduction zones, raises new
9 questions on the genesis of abiotic hydrocarbons at convergent margin and its impact on the
10 deep carbon cycle. High-pressure ultramafic bodies exhumed in metamorphic belts can
11 provide insights on the mechanisms of high-pressure serpentinization in subduction zones
12 and on the chemistry of the resulting fluids. This study focuses on the ultramafic Belvidere
13 Mountain complex belonging to the Appalachian belt of northern Vermont, USA.
14 Microstructures show overgrowth of both primary (Mg# 0.91) and metamorphic (Mg# 0.95)
15 olivine by delicate antigorite crystals, pointing to at least one stage of serpentinization at high-
16 temperature conditions and consistent with the high-pressure subduction evolution of the
17 Belvidere Mountain complex. Formation of ubiquitous magnetite and local Fe-Ni alloys
18 testifies to the partial oxidation of Fe²⁺ into Fe³⁺ and generation of reduced conditions. Fluid
19 inclusion trails cross-cutting the primary olivine relicts suggest their formation during the
20 antigorite serpentinization event. MicroRaman spectroscopy on the fluid inclusions reveals a
21 CH₄-rich gaseous composition, as well as N₂, NH₃ and H₂S. Moreover, the precipitation of
22 daughter minerals such as lizardite and brucite in the fluid inclusions indicate the initial
23 presence of H₂O in the fluid. High-pressure serpentinization driven by the infiltration of

24 metasediment-derived aqueous fluids is proposed at the origin of CH₄ and other reduced fluid
25 species preserved in the fluid inclusions. This suggests the Belvidere Mountain complex as an
26 example of deep abiotic hydrocarbon genesis related to high-pressure serpentinization in an
27 early Paleozoic subduction zone.

28 **Keywords:** HP Serpentinization, Metamorphic olivine, Abiotic methane, C fluxes at
29 subduction zones, Belvidere Mountain Complex.

1 Introduction

2 Alteration of ultramafic rocks by aqueous fluids, or serpentinization, produces serpentine-rich
3 rocks and may be accompanied by redox reactions leading to the formation of H_2 and abiotic
4 light hydrocarbons (Mével, 2003; Moody, 1976; Seyfried Jr et al., 2007). Oxidation of Fe^{2+} in
5 mantle minerals and formation of Fe^{3+} minerals such as magnetite produces H_2 , which may
6 then promote the conversions of dissolved carbon-bearing species into abiotic CH_4 (Andreani
7 et al., 2013; Berndt et al., 1996). Serpentinization is well documented at mid-ocean ridges and
8 on land (Andréani et al., 2007; Cannat et al., 2010; Etiope et al., 2011; Klein et al., 2014;
9 Schrenk et al., 2013), where H_2 and CH_4 produced through serpentinization can support
10 biological communities and could be linked to the emergence of early life on Earth (Kelley et
11 al., 2005; Ménez et al., 2018; Sleep and Bird, 2007). Serpentinization processes may also
12 happen at much greater depths and affect subducted mantle sections and the overlying
13 mantle wedge at convergent margins (Guillot et al., 2015, 2000; Vitale Brovarone et al., 2017;
14 Wada et al., 2008), owing to the availability of aqueous fluids (Bebout and Penniston-Dorland,
15 2016; Deschamps et al., 2013). However, the patterns of serpentinization reactions at high-
16 temperature (HT) and high-pressure (HP) conditions, here defined with respect to the
17 serpentine stability field, and the associated fluid-rock redox budgets are still largely
18 unconstrained. The possibility that HT-HP serpentinization may not involve Fe oxidation and
19 genesis of H_2 has been proposed (Evans, 2010). However, natural case studies of slab-derived
20 serpentinized peridotites suggest that magnetite, H_2 and abiotic CH_4 can be produced at these
21 conditions (Vitale Brovarone et al., 2020). Ultramafic bodies in metamorphic belts can provide
22 good insights on the mechanisms of HP-HT serpentinization and the resulting fluids (Evans et

al., 2017), and therefore make good case studies for the investigation of the mechanisms of serpentization in subduction zones.

The Belvidere ultramafic complex, Vermont, USA, is a fragment of the Iapetus ocean that was involved in the Taconic orogeny and recorded HP metamorphism during Cambrian-Ordovician (Chew and van Staal, 2014; Gale, 1980; Honsberger et al., 2017). This complex includes variably serpentized peridotites bearing antigorite, the HT serpentine polymorph stable at subduction zone HP conditions (Schwartz et al., 2013), therefore making a potential example of HT-HP serpentization. In this work, we integrate field, microstructural, thermodynamic, and fluid inclusions data to investigate the patterns and timing of serpentization of the Belvidere ultramafic complex, with particular focus on the HP fluid-rock interactions recorded by these rocks.

1. Geologic setting

The Belvidere Mountain complex (BMC) area is part of a North-South trending belt of mafic/ultramafic rocks belonging to the Appalachian Mountain system and extending from Newfoundland to Georgia (Gale, 2007; Hibbard et al., 2006) (Fig. 1). These ultramafic bodies mainly consist of variably serpentized peridotites, and associated metabasic and metafelsic rocks tectonically embedded within Cambrian-Ordovician metasedimentary and metavolcanic formations (Chidester et al., 1978; Gale, 1986, 1980; Laird et al., 1984; Van Baalen et al., 2009). The BMC, as well as other mafic/ultramafic complexes such as the Tillotson Peak and the Pennington complexes, are interpreted to represent remnants of an ocean-continent transition zone associated with the extension of the Laurentian margin (Chew and van Staal, 2014). These terranes were successively involved in the closure of the

Iapetus Ocean during the Ordovician Taconic orogeny (Doolan et al., 1982; Honsberger et al., 2017; Karabinos et al., 1998; Laird et al., 1984; Stanley et al., 1984). The BMC forms a 6.5 km long body that structurally overlies the metasedimentary Ottauquechee and Stowe Formations to the East and is overlain by the Hazen Notch formation to the West. The Stowe Formation is late Cambrian, composed of gray-green quartz-chlorite-sericite +/- magnetite schists. The Ottauquechee Formation is middle Cambrian consisting carbonaceous pyritiferous phyllite. The Hazen Notch Formation is dated from Neoproterozoic to Cambrian, graphitic and non-graphitic quartz-albite-sclerite-chlorite schist, along medium-grained, massive, quartz-albite-muscovite gneiss. The internal architecture of the BMC comprises, from top to bottom, variably serpentinized dunite and harzburgite, coarse-grained and fine-grained amphibolite, greenstone, muscovite schist, and albite gneiss (Gale, 1986, 1980; Van Baalen et al., 2009). Lenticular bodies composed of talc-carbonate rocks and steatite, often including cores of relatively unserpentinized peridotite, are observed within the BMC, and range size from a few meters to several tens of meter (Chidester et al., 1978). The BMC rocks underwent Taconic blueschist-facies peak metamorphic conditions constrained at 0.9-1.3 GPa and 510-520 °C in metabasic rocks (Honsberger, 2015; Laird et al., 1993). Slightly higher P, blueschist-to-eclogite-facies metamorphic conditions are recorded by the Tilliston Peak mafic rocks located just north of the BMC (Laird et al., 1993, 1984). This tectonometamorphic event has been dated at 505-473 Ma by $^{40}/^{39}\text{Ar}$ amphibole and mica geochronology (Castonguay et al., 2012; Laird et al., 1993).

2. Methods

Quantitative energy-dispersive X-ray spectroscopy (EDS) analyses and backscattered electron (BSE) imaging were carried out using the JSM-IT300LV Scanning Electron Microscope Oxford

68 Inca Energy Dispersive Spectrometer at the Department of Earth Sciences of Turin University.
69 Data were processed with the INCA software from Oxford Instruments. Quantitative analysis
70 employed 15kV accelerating voltage and 20 s to 40 s counting time. Natural and synthetic
71 mineral and oxide standards were employed. EDS calibration was made using Cobalt
72 standard.

73 Quantitative wavelength-dispersive spectrometer (WDS) analyses were carried out using a
74 JEOL 8200 Super Probe at the Department of Earth Sciences “Ardito Desio” of Milan
75 University. The microprobe was using a 15keV accelerating voltage under 5 nÅ, with 30s
76 counting time under maximum emission peak. Sixteen oxide composition were measured,
77 using synthetic and natural standards: grossular (Si, Al and Ca), omphacite (Na), K-feldspath
78 (K), fayalite (Fe), forsterite (Mg), rhodonites (Mn), niccolite (Ni), ilmenite (Ti), galena (Pb and
79 S), pure Cr, pure Zn and pure Cu.

80 MicroRaman spectroscopy of minerals and fluid inclusions was done at the Department of
81 Earth Sciences, University of Turin, with a LabRAM HR (VIS) (HORIBA Jobin Yvon) equipped of
82 a 532.11 nm, solid-state Nd laser, a Super Notch Plus filter with spectral resolution of 1 cm⁻¹,
83 and a grating of 600 grooves/mm. The laser of emission power was set at 80 mW and focused
84 to 5 µm with a ×100 objective with a laser power on the sample < 5 mW. Calibration was
85 performed using the 520.6 cm⁻¹ band of a silicon standard for the 100-2000 cm⁻¹ range, and
86 the 2331 cm⁻¹ band of atmospheric N₂ for the 2000-4000 cm⁻¹ range. Four accumulations of
87 30–60 s were collected for each spectrum. Raman spectra of fluid inclusions were performed
88 on double-polished thick sections unless otherwise specified.

Isotopic composition measurements of methane were performed on a MAT 253 (Thermo Fisher) mass spectrometer, coupled with gas chromatography (GCC-IR-MS) in order to purify the samples. The gas phase was extracted and measured after crushing the rock sampler under vacuum.

Thermodynamic modelling was performed using the Deep Earth Water (DEW) Model (Sverjensky et al., 2014) and the EQ3/EQ6 software (Wolery and Jarek, 2003) with a modified Berman database (Berman, 1988). EQ3 was used to calculate the composition of a fluid in equilibrium with a given mineral assemblage as, fO_2 , P and T. EQ6 was used to model the interaction of fluid compositions from EQ3 with another mineral assemblage as function of the fluid/rock (F/R) ratio.

3. Sample description and mineral chemistry

In this section, we present the petrography, microstructures and mineral chemistry of samples collected in the Belvidere mine (Fig. 2) and showing different degrees of serpentinization. The selected samples range from weakly serpentinized dunite (V18-2a and V18-2b) to partially serpentinized dunite including layers of boudinaged meta-pyroxenite (V18-3a and V18-3b), to fully serpentinized peridotite (V18-B3).

3.1. Microstructural characterization

Sample V18-2a (least serpentinized dunite) consists of olivine (~80 vol.%), antigorite (~10 vol.%), Cr-spinel (>5 vol.%), magnetite (<5 vol.%), chlorite (<1 vol.%), sulphides (<1 vol.%), and alloys (<1 vol.%) determined from visual estimate in thin section. Primary olivine forms crystals ranging in size from 0.25 to 1 mm (Fig. 3A). It is partially replaced by antigorite, as

identified by MicroRaman spectroscopy (Fig. 4), along mesh-like structures (Fig. 3A-C). Antigorite is present as elongated crystals, up to 200 μm in length, which statistically overgrew the olivine (Fig. 3C). Magnetite is present in three microstructural domains: as large, millimeter scale crystals rimming chromite relicts, as grains of $\sim 50\ \mu\text{m}$ in the mesh structures, and as millimeter scale crystals in antigorite veins. Chlorite is found, together with magnetite, around Cr-spinel relicts (Fig. 3B).

Sample V18-2b (serpentinized dunite) consists of antigorite ($\sim 40\ \text{vol.}\%$), olivine ($\sim 40\ \text{vol.}\%$, including primary and metamorphic olivine), magnetite ($>5\ \text{vol.}\%$), chlorite ($>5\ \text{vol.}\%$), brucite ($<5\ \text{vol.}\%$), and alloys ($<1\ \text{vol.}\%$). The structure is similar to V18-2a, but in this case the extent of serpentinization along the meshes is higher. SEM backscattered-electron imaging reveals the presence of a second generation of olivine, hereafter metamorphic olivine (see Section 4.2 for discussion) growing in two different sites: epitaxially on the primary olivine and replacing former orthopyroxene (Fig. 5A-B). Striped zoning is observed in primary olivine (Fig. 5A), as described in Plümper et al., 2012a, alternating thin forsterite-richer and forsterite-poorer olivine composition. The initial presence of orthopyroxene in the rock is inferred based on the presence of clinopyroxene exsolutions preserved in metamorphic olivine-rich pseudomorphoses (Fig. 3D and 5B). Antigorite is present as elongated (0.5 mm in length) crystals and as fine-grained aggregates in the matrix. The elongated antigorite crystals are chemically zoned, with bright core and dark rim in backscattered electron imaging (Fig. 5A). Raman spectra of both generations exhibit the characteristic $1043\ \text{cm}^{-1}$ band of antigorite, whereas the main OH stretching is at $3664\ \text{cm}^{-1}$ in the bright core and at $3673\ \text{cm}^{-1}$ in the dark rim (Fig. 4C), both inconsistent with antigorite-lizardite mixing. The higher Raman shift of the dark rim may be linked to variation of pressure condition (Auzende et al., 2004). The dark

antigorite generation appears the same forming the fine-grained aggregates. The bright antigorite generation (at the core of large crystals) is never found in contact with either primary or metamorphic olivine, whereas the darker antigorite generation (at the rim of large crystals of disseminated in the matrix) is in contact with them (Fig. 5A). Magnetite is more abundant relative to sample V18-2a, especially along meshes. Brucite was identified by SEM and Raman (Fig. 4D) in veins, sometimes associated with metamorphic olivine (Fig. 5C). Alloys and sulphides are present in association with antigorite and are locally associated to magnetite (Fig. 5D).

Samples V18-3a and 3b are from a boudinaged layer of clinopyroxenite included in an intensely serpentinized dunite (Fig. 3E-G). The mineral assemblage and microstructures of the serpentinized dunite part of the sample is similar to sample V18-2b, yet more intensely serpentinized. The primary clinopyroxene is fully replaced by diopside aggregates in both the clinopyroxenite layer and the host dunite. The primary clinopyroxene sites in this sample are slightly different from the serpentinized dunite, with less abundant magnetite and characteristic fan-shaped diopside aggregates in the former compared to the latter. Metamorphic olivine is present at the rim of primary clinopyroxene and along its cleavages, together with antigorite (Fig. 5E-F). In the latter case, metamorphic olivine is localized along thin arrays encircled by antigorite (Fig. 5F). Antigorite shows the same chemical zoning as observed in the dunite, with brighter cores and darker rims in backscatter electron imaging (Fig. 5G). Backscattered electron imaging reveals that the dark antigorite shows similar overgrowth microstructural relationships with both primary and metamorphic olivine (Fig. 5E). The microstructures reflect either equilibrium between antigorite and the two olivine generations, or overgrowth of both olivine generations by the antigorite. Considering that the

amount of primary olivine strongly decreases in favour of antigorite in several samples, which suggests serpentinization of the primary olivine, second antigorite generation formed after the growth of metamorphic olivine appears. It is possible, even though the microstructures could not confirm it, that the first antigorite generation grew prior to or together with the metamorphic olivine. Magnetite is present in four different structural sites: as arrays of ~ 50 μm size crystals along the meshes, as trails of ~ 50 μm crystals in primary olivine and clinopyroxene pseudomorphoses, as aggregates rimming the primary Cr-spinel, and as millimeter scale aggregates along discordant veins. The Cr-spinel sites are characterized by three different layers: a rather preserved core, a mantle of ferritchromite, and a rim of magnetite (Fig. 5E; see Section 4.2).

Sample V18-B3 is a fully serpentinized peridotite. The matrix is composed of a mixture of antigorite and chrysotile (identified by MicroRaman) with magnetite. Brucite is observed replacing pyroxene sites and is associated with magnetite and/or metamorphic olivine (Fig. 3H and 5H). Based on the microstructural observations on sample V18-2b, these pseudomorphoses are interpreted as former orthopyroxene crystals replaced by metamorphic olivine and successively hydrated to form serpentine + brucite \pm magnetite.

3.2. Mineral chemistry

Primary olivine has Mg# of 0.91-0.92 [$\text{Mg\#} = \text{Mg}/(\text{Fe}+\text{Mg})$], whereas metamorphic olivine is enriched in Mg (Mg# of 0.95) (Table 1, Fig. 6). The Mn# [$\text{Mn\#} = \text{Mn}/(\text{Mn}+\text{Fe}+\text{Mn}+\text{Ni})$] of metamorphic olivine (0.0040 ± 0.0006) is much higher than primary olivine (0.0015 ± 0.0005). Metamorphic olivine analyses in sample V18-B3 show slightly lower Mg# and higher Mn# content relative to metamorphic olivine from other samples. Metamorphic olivine rimming

the primary orthopyroxene sites in sample V18-3a has higher CaO content (0.25 wt.%) compared to the metamorphic olivine overgrowing primary olivine in V18-2b (0.02 wt.%). Metamorphic olivine in the sample V18-B3 show slightly lower Mg# and highly increased MnO content (1.2 wt %) in regard to metamorphic olivine from other samples. The NiO content of primary olivine (0.38 to 0.49 wt.%) and metamorphic olivine (0.39 to 0.46 wt.%) are similar.

The incorporation of Mn in olivine appears to be characteristic of metamorphic olivine from several localities regardless of the olivine formation environments (dehydration vs. hydration). The Mg# of metamorphic olivine relative to primary olivine may depend upon several parameters such as the stability of different Fe-bearing minerals, the Fe partitioning among them, and the P-T and redox conditions (Frost and Beard, 2007; Majumdar et al., 2016; Nozaka, 2018, 2003). An increase in Mg# (and MnO) in metamorphic olivine relative to primary olivine has been observed in inferred mantle wedge peridotites recording HP serpentinization (Dandar et al., 2019; Guillot et al., 2000). Plümper et al., 2012a report striped Mg# zoning in hydrated supra-subduction mantle rocks as the result of chemical interaction during antigorite serpentinization at high temperature conditions. Metamorphic olivine formed through prograde antigorite + brucite dehydration shows either lower or higher Mg# compared to mantle olivine (Arai et al., 2012; Debret et al., 2013; Iyer et al., 2008; Kempf and Hermann, 2018; Nozaka, 2018; Plümper et al., 2012b; Scambelluri et al., 1995; Shen et al., 2015)(Fig. 6).

The core of individual, elongated antigorite crystals exhibits higher FeO (1.6 to 2.6 wt.% [Mg# 0.94-0.96]), Al₂O₃ (1.77 wt.%) [Mg# =Mg/(Mg+ΣFe)], and Cr₂O₃ (0.61 wt.%) than the rim (1.35 wt.% [Mg# 0.97], 0.52 wt.%, 0.13 wt.%, respectively) (Table 1). Unzoned matrix antigorite has

a composition equivalent to the rim of the elongated antigorite crystals. The Mn# [$\text{Mn\#} = \text{Mn}/(\text{Mn}+\text{Fe}+\text{Mn}+\text{Ni})$] of antigorite is 0.0006 (± 0.0004).

The preserved spinel core has Cr# [$\text{Cr}/(\text{Cr}+\text{Al})$] of 0.79 (Table 2). The mantle overgrowing the primary spinel has a ferritchromite mantle of Cr-magnetite with a Cr# of 0.91 and higher MnO relative to the core. The magnetite rims with no Al_2O_3 , but high Cr_2O_3 (1.87 wt.%). The composition of magnetite in the meshes and veins differs from magnetite found in the spinel sites, with very little Cr_2O_3 .

Diopside has a Mg number [$\text{Mg\#} = \text{Mg}/(\text{Mg}+\text{Fe})$] of 0.98. Chlorite has an Mg# [$\text{Mg\#} = \text{Mg}/(\text{Mg}+\Sigma\text{Fe})$] of 0.95, and Cr_2O_3 up to 4.07 wt.% (Table 1).

Brucite has up to 3 wt.% FeO (as total Fe), Mg# [$\text{Mg\#} = \text{Mg}/(\text{Mg}+\text{Fe})$] of 0.97 (Table 2). Alloys and sulfides are Ni rich, with various amounts of S, Fe and trace amounts of Pb, Cu, et Co (Table 3). Alloys mainly consist of Cu-bearing FeNi alloy (taenite) (Table 3). Sulphides include Ni, Cu, and Fe sulphides. Only heazlewoodite (NiS) was analysed whereas for other sulphides proper analyses could not be obtain owing to the small grain sizes.

3.3. Fluid inclusion analysis

Primary olivine in all samples is rich in fluid inclusions forming secondary trails (Fig. 7). The fluid inclusion trails are confined within individual crystals and show two alternative structural relationships relative to the antigorite veins, being either cut by them (Fig. 7A) or injected from them (Fig. 7B-C). These patterns suggest a secondary fluid trapping during the antigorite serpentinization event forming the main mesh structure observed in the rock.

Fluid inclusions exhibit rounded to elongated shapes (Fig. 7D-E). Optical microscope observations at room conditions suggest that the fluid inclusions are either single-phase and gaseous, or bi-phase with solid and gas. MicroRaman spectra of fluid inclusions are presented in Fig. 8. The spectra show the presence of marked CH₄ bands (2912 cm⁻¹), as well as N₂ (2327 cm⁻¹), NH₃ (3324 cm⁻¹), S-H/H₂S (2575 cm⁻¹). Free H₂O in the fluid inclusions was not detected by MicroRaman. However, the presence of tiny amounts of free H₂O in the fluid inclusions — undetectable by MicroRaman at room conditions — cannot be excluded (Berkesi et al., 2009; Lamadrid et al., 2017).

The molar fraction of gas in the gas mixture was estimated using the Raman scattering cross-section and the instrumental efficiency of each species. Using equation presented in Frezzotti *et al.*, 2012, we obtain the following molar proportion: CH₄ = 92±6%, N₂ = 6±5%, H₂S = 1±1% and NH₃ = 1±2% for the mean composition of twenty inclusions in olivine from all samples (Fig 9). Composition within the same inclusion trail show molar fractionation variation smaller than 1% but different trail within the same crystal can exhibit up to 10% of molar fraction of CH₄ and could reflect fluid heterogeneity. Alternatively, this effect can be the result of different crystal orientation during data acquisition (Caumon et al., 2019). No clear pattern was observed linked to relationship between inclusion trails and antigorite veinlets.

Solid phases were identified in large fluid inclusions. MicroRaman analysis revealed the presence of lizardite and brucite but no magnetite was detected. Some inclusions contain graphite as a solid phase in the inclusion in addition (Fig. 7F and Fig. 8B). The only sporadic presence of graphite in the fluid inclusions, and in particular in inclusions resulting from necking processes, suggest that this mineral precipitated as a result of local respeciation of the fluid inclusions (Cesare, 1995). The presence of hydrous phases in the inclusions suggests

re-equilibration of the inclusion with the host mineral, effectively serpentinizing the olivine and consuming water initially present in the inclusions. However, the presence of step-daughter minerals in the inclusion is not systematic, suggesting that the initial fluid was already rich in CH_4 ($-\text{N}_2$ - NH_3 - H_2S) at the time of trapping, and that the reduced fluid species did not form only inside the fluid inclusions.

3.4. Rodingite

Rodingite are ultramafic rocks that are composed of carbonate, garnet, diopside, epidote \pm graphite. While not being the focus of this study, the carbonate in the rodingite bear numerous trails of fluid inclusions. Fluid inclusions exhibit negative crystal shape and are single-phase gaseous. The composition of the carbonate-hosted fluid inclusions, as revealed by Raman spectroscopy, is essentially CH_4 and N_2 . Using quantitative estimation of inclusions in carbonates (see section 4.3) yield molar fractions of $\text{N}_2 = 67 \pm 4\%$, $\text{CH}_4 = 33 \pm 4\%$ on four different inclusions.

3.5. Thermodynamic modelling

Thermodynamic calculations were performed in order to constrain the mineralogical, fluid and redox pattern of the HP serpentinization. Because the selected partially serpentinized samples are comprised in strongly serpentinized rocks and embedded in metasediment, two fluid equilibriums can be considered. For silica-rich fluid sources (e.g. metasedimentary rocks or talc-bearing ultramafic rocks), the predicted assemblages do not match the natural samples. For this reason, the fluid composition calculated with EQ3 was equilibrated with a serpentinite consisting of antigorite + magnetite + brucite + chlorite + olivine. This fluid then reacted with a dunite with mineral modal proportions comparable with the study samples

and consisting of 92% olivine (forsterite 90%, fayalite 10%), 5.4% orthopyroxene (enstatite 90%, ferrosilite 10%), 2.5% clinopyroxene (diopside 90%, hedenbergite 10%) and 0.1% spinel. The fO_2 of the infiltrating fluid was set at the quartz-fayalite-magnetite (QFM) buffer. The calculations were done at temperatures consistent with the peak metamorphic conditions estimated for the BMC, i.e., 400 °C to 500 °C and 1 GPa (Honsberger, 2015; Laird et al., 1993), and for different F/R ratios. Figure 10 shows the mineralogical evolution as a function of reaction progress at 450 °C and 1GPa for a fluid rock ratio of 1. The model reaction proceeds with progressive transformation of, from the first to the last reacting mineral, mantle spinel, clinopyroxene, orthopyroxene, and olivine. Magnetite starts to form during the early stages of the reaction along with chlorite in response to spinel consumption. Reaction of mantle pyroxenes marks the precipitation of metamorphic clinopyroxene (diopside 93%, hedenbergite 3.35% and clino-enstatite 3.65%), metamorphic olivine, antigorite, and additional magnetite. The late formation of antigorite marks the partial consumption of metamorphic olivine and a decrease in its Mg#, from Mg# 0.90 to Mg# 0.83. These patterns reflect the microstructural features observed in the natural samples. For example, spinel appears intensely replaced by chlorite in rather unserpentinized portions of the rock (Fig. 10A). Similarly, mantle olivine adjacent to fully replaced mantle pyroxenes is commonly little affected by the serpentinization. Both mantle and metamorphic olivine in the natural samples appear texturally replaced by antigorite, as also suggested by the modelling while approaching equilibration. With the chosen bulk composition and used thermodynamic data set, the formation of antigorite is limited to $T < 470$ °C. The antigorite stability field could be enlarged by considering iron in the antigorite thermodynamic model. The fO_2 decreases progressively during the reaction progress, with a steep decrease during the formation of antigorite down to $\Delta\text{Log QFM} = -1.2$ (Fig. 10C). Methane, initially about 1 order of magnitude

less concentrated than CO₂ in the reacting fluid, becomes a dominant species at reaction completion (about 1 order of magnitude more concentrated than CO₂). Nevertheless, variations of parameters such as F/R ratio, mineralogy, or temperature, were found to affect the proportion of CH₄ and CO₂. As an example, increasing the modal proportion of either orthopyroxene or clinopyroxene in the initial rock or decreasing the F/R ratio appears to favour a higher proportion of CH₄ in the fluid in respect to CO₂. The model predicts high relative concentration of H₂ in the fluids, however H₂ was not detected in natural samples by micro-Raman spectroscopy. Sulphur and nitrogen speciation were also assessed, with HS⁻ and H₂S and NH₃ being the dominant sulphur species relative to HS O₄⁻ and N₂ and N H₄⁺, respectively (Fig. 10B).

4. Discussion

4.1. Patterns and timing of serpentinization

The timing of serpentinization of slab-derived, exhumed HP serpentinized rocks can span (sub)seafloor conditions prior to subduction, prograde hydration during subduction, or retrograde hydration during exhumation. The BMC complex has been interpreted as a fragment of subducted Iapetus lithosphere, and therefore may have recorded different stages of serpentinization. Although the possibility of at least some (sub)seafloor serpentinization prior to the Taconic subduction cannot be excluded, our data cannot provide any proof of such a pre-subduction event and, instead, suggest a main hydration event at HP-HT conditions in the subduction zone.

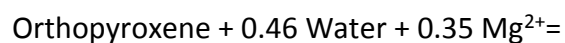
Besides late chrysotile veinlets, antigorite is the only serpentine polysome identified in the BMC rocks. Although formation of antigorite may occur in a wide range of P-T conditions also as a function of chemical parameters such as the silica activity (Rouméjon et al., 2019),

serpentinites dominated by antigorite are generally referred to the HT temperature part of the serpentine stability field, generally above ~300-400 °C (Evans, 2004; Schwartz et al., 2013). In most subduction zone settings, these conditions also correspond to relatively HP conditions above 1 GPa. However, the presence of antigorite does not necessarily imply the serpentinization event to have happened at HP-HT conditions because it could also have formed as a result of the prograde transformation of lizardite or chrysotile following the reaction:

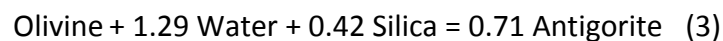


Nevertheless, several lines of evidence indicate that the BMC rocks recorded a stage of HP-HT serpentinization. As a first general consideration, the presence of fresh mantle assemblages throughout the complex (Chidester *et al.*, 1978; this study) represents a suitable condition to promote HP-HT serpentinization in the subduction zone, if aqueous fluids are available. Such a process has already been proposed in other HP ultramafic massifs preserving fresh mantle assemblages (e.g. Fröh-Green et al., 2004; Scambelluri and Tonarini, 2012; Vitale Brovarone et al., 2020, 2017). The BMC rocks provides evidence for such a HP hydration event. Figure 11 summarizes the proposed fluid-rock evolution of the BMC rocks as inferred from the studied samples. The first indication of serpentinization (stage I in Fig. 11) is suggested by the growth of elongated metamorphic olivine on the primary clinopyroxene sites (Fig. 5G), which suggests the former presence of serpentine blades overgrowing the primary clinopyroxene. The selective growth of serpentine at the expense of clinopyroxene rather than primary olivine places this hypothetical event at HT conditions (Klein et al., 2013) and possibly in the antigorite stability field (Fig. 12). Metamorphic olivine is most commonly interpreted to form in response of serpentine dehydration during prograde metamorphism

(Plümper et al., 2017; Scambelluri et al., 1991). Figure 12 provides a compilation of traditional serpentine dehydration reactions leading to the formation of metamorphic olivine. The peak metamorphic conditions proposed for the BMC (0.9-1.3 GPa and 520 °C) are consistent with the first olivine-forming reaction involving antigorite + brucite as reactants. Moreover, several studies have shown that olivine can form at T conditions lower than the reactions shown in figure 12 as a result of local bulk compositional features (Plümper et al., 2017). Alternatively, metamorphic olivine after orthopyroxene may also have formed in response to hydration rather than dehydration reactions, as already proposed for serpentinized mantle wedge rocks (Dandar et al., 2019) following the reaction:



Followed by the hydration of olivine to form antigorite following the reaction



In either case (hydration or dehydration), the amount of serpentinization predating the formation of metamorphic olivine must have been very low and, if any, related to a HT event.

The second, more robustly constrained stage of transformation (stage II in Fig. 11) is characterized by the formation of metamorphic olivine after primary orthopyroxene, and as rim around primary clinopyroxene (now recrystallized into diopside). This reaction was observed in rocks containing rather undisturbed primary olivine, which again point to HT serpentinization conditions (Klein et al., 2013). The partial preservation of clinopyroxene exsolution lamellae inside metamorphic olivine pseudomorphic on orthopyroxene may suggest nearly isovolumetric replacement during this event (Plümper et al., 2012b; Viti et al.,

2005). The thermodynamic modeling results suggest that, at 450 °C and 1 GPa, a transient antigorite generation may have formed together with metamorphic olivine early in the fluid-rock interaction, along with spinel breakdown. The Al-Cr-rich antigorite cores (Atg1) observed in the studied samples may testify to this transient antigorite formation. The application of empirical distribution coefficient K_D for antigorite and olivine by Evans, 2008 and Trommsdorff and Evans, 1974 support this hypothesis (Table 4). The empirical Mg distribution coefficient K_D [antigorite/olivine, $K_D = (\Sigma Fe/Mg_{Srp})/(Fe/Mg_{Ol})$] proposed by Evans, 2008 is 0.45-0.35 upon consideration of ferric iron in the antigorite. The Atg1/metamorphic olivine apparent K_D is 0.49-0.25, which agrees with the value proposed by Evans, 2008 for equilibrium, compared with other antigorite/olivine pairs (Atg1/primary olivine = 0.14-0.25; matrix antigorite (Atg2)/primary olivine = 0.11; Atg2/metamorphic olivine = 0.17-0.25). The Mn distribution between antigorite and olivine gives similar results. The empirical Mn distribution coefficients for antigorite/olivine equilibria is 0.18 (Trommsdorff and Evans, 1974). The Atg1/metamorphic olivine pair has apparent K_D of 0.14-0.18, thus consistent with the predicted equilibrium (Table 4).

The third stage (stage III in Fig. 11) is characterized by the growth of a matrix antigorite (Atg2) at the expense of both primary and metamorphic olivine. This event may mark either retrograde hydration along the exhumation path of the BMC, or the progression of the fluid-rock interaction. As indicated by the thermodynamic modeling results, a second antigorite generation is expected to form at 450 °C and 1 GPa after the precipitation of metamorphic olivine (Fig. 10A). The modeling predicts this second antigorite and metamorphic olivine to be stable together. However, the apparent K_D for matrix antigorite and metamorphic olivine suggest disequilibrium (equilibrium Mg K_D = 0.45, measured = 0.17-0.25; equilibrium Mn K_D =

0.18, measured = 0.09-0.14) (Table 4). This feature suggests that stage III marks the beginning of retrograde hydration.

The fourth stage of serpentinization (IV in Fig. 11) is characterized by the complete serpentinization of primary olivine and partial to full serpentinization of metamorphic olivine. The partial preservation of metamorphic olivine after orthopyroxene in sample free of any primary olivine relict indicates that the largest event of serpentinization of the BMC rocks took place after the formation of metamorphic olivine. The presence of both antigorite and lizardite + brucite at the expense of metamorphic olivine after orthopyroxene suggests that this event protracted during the cooling of the BMC metamorphic path to temperatures lower than 400 °C (Fig. 12).

In summary, based on the collected petrographic and thermodynamic data, the dominant serpentinization event observed in the BMC complex is interpreted to have taken place in the Taconic subduction zone.

4.2. Timing of fluid inclusion formation and origin of CH₄

4.2.1. Timing of fluid inclusion entrapment

Fluid inclusions in the BMC ultramafic and related metasomatic rocks contain reduced fluid species such as CH₄, NH₃, and H₂S. The timing of fluid inclusion formation, as well as the origin of their reduced speciation, is discussed in this section.

Reduced fluids have been found to form in ultramafic systems in a wide range of geologic conditions spanning mid-ocean ridges, obducted ophiolitic massifs, and orogenic peridotite bodies, in subduction, and in the upper mantle (Andréani et al., 2007; Etiope et al., 2011;

Schrenk et al., 2013). In the BMC rocks, the fluid inclusions may have formed in three different stages of the evolution of the massif and corresponding to three different geodynamic settings: (i) in the mantle prior to the formation of the Iapetus Ocean, (ii) during the (sub)seafloor evolution prior to subduction, and (iii) in the subduction zone.

A primary mantle origin can be ruled out because the observed fluid inclusions occur as secondary trails propagating from the antigorite veinlets crossing olivine crystal. A (sub)seafloor origin would match the identification of CH₄-rich fluid inclusions in oceanic peridotite (Cannat et al., 2010; Holm and Charlou, 2001). However, in this case, the fluid inclusions would have been preserved during prograde metamorphism to at least 520 °C and 1 GPa, which is unlikely (Touret, 2001). Moreover, the BMC fluid inclusions are rich in N species (NH₃, N₂), which seems to be an uncommon feature in fluid inclusions from oceanic peridotites (Grozeva et al., 2020; Klein et al., 2019). Instead, N-rich, NH₃-bearing fluid inclusions have been recently documented in CH₄-rich fluid inclusions in HP serpentized peridotites from the Alpine belt and proposed to represent a distinctive feature of subduction zone serpentizing fluids relative to mantle or (sub)seafloor fluids, especially in the presence of metasediment-derived fluids (Vitale Brovarone et al., 2020). Considering the microstructural and petrologic features discussed in Section 5.1, and the abundance of N species, a metamorphic origin in the Taconic subduction is proposed for the studied fluid inclusions.

The formation of lizardite and brucite as step-daughter minerals inside the fluid inclusions can be interpreted (1) as a prograde, pre-antigorite inclusion-host interactions, (2) as a retrograde reequilibration of antigorite during cooling of the BMC below ~400 °C with excess brucite (Reaction 1), or (3) as a retrograde host-inclusion interaction below ~400 °C (Fig. 12).

Excluding lizardite (meta)stability due to local equilibrium/kinetic features or faster antigorite-lizardite conversion in the inclusions relative to the host rock, we interpret the formation of step-daughter lizardite and brucite as a retrograde host-inclusion interaction. Similar interpretations have been proposed for analogous inclusions from Alpine belt (Vitale Brovarone et al., 2020).

4.2.2. Origin of the reducing potential and fluid sources

Another important question is the origin the identified reduced fluids species. In particular, several studies over the last decades have investigated the biotic or abiotic origin of geological CH₄ and associated reduced fluid species (Etiope et al., 2011; Etiope and Sherwood Lollar, 2013; McCollom, 2016; Ménez et al., 2018). Ultramafic systems are generally favourable environments for the genesis of abiotic CH₄ (Section 5.2.1), but other interpretations are also possible.

For example, the abundance of metasedimentary rocks in the study area may have promoted the formation of thermogenic gases during their prograde evolution. This hypothesis would be also consistent with the production of NH₃ through degassing of organic matter in metasedimentary rocks (Bebout and Fogel, 1992; Li et al., 2009). Biotic processes, including thermogenic gas formation, typically show very light $\delta^{13}\text{C}_{\text{CH}_4}$ signatures (Etiope and Sherwood Lollar, 2013), whereas abiotic processes generally result in much heavier $\delta^{13}\text{C}_{\text{CH}_4}$ (~-50 to 0‰) (Etiope and Sherwood Lollar, 2013). In order to test this hypothesis, we performed reconnaissance $\delta^{13}\text{C}$ analysis of CH₄ in the fluid inclusions (Boutier et al., in preparation). The analyses yielded $\delta^{13}\text{C}$ in the range of -14‰ ($\pm 2\%$) for inclusions in olivine, and -13‰ ($\pm 1\%$) for carbonate-hosted methane-rich inclusions from the rodingite. Even though these results

must be considered as preliminary test data, they seem to exclude the possibility of a pure thermogenic source.

Following the hypothesis of an abiotic origin, two possible mechanisms for the formation of CH₄ can be considered with either external or internal sources, respectively. External sources correspond to the infiltration of CH₄ and other reduced species formed abiotically in other geological reservoirs. A deep mantle origin for the reduced fluids detected in the BMC fluid inclusions appears unlikely if the syn-inclusion, water-rich nature of the serpentinizing fluid is considered. The metasedimentary formations adjacent to the BMC contain carbonate, graphitic carbon, sulphides, and phyllosilicates as potential sources of the C-N-S-H fluid identified in the fluid inclusions. Previous studies along the Appalachian belt have reported evidence of carbon mobilization from these metasedimentary formations or their along-strike equivalents. For example, Zhang *et al.*, 2018 documented metamorphic loss of isotopically light carbon from the Wepawaug schists, Connecticut. The possibility for these carbonate-bearing formations to generate strongly reduced fluids abiotically is not obvious —for reference, water-maximum conditions in graphite-saturated fluids contain roughly equal proportions of CH₄ and CO₂ (Connolly, 1995; Holloway, 1984) —. Nevertheless, evidence for the circulation of CH₄-rich fluids in equivalent formations in East Central Vermont and New Hampshire has been reported (Evans *et al.*, 2002; Rumble III and Hoering, 1986). Nevertheless, most petrological studies focusing on New England metasediment-derived fluids point to more oxidized, CO₂-dominated aqueous fluids (Ferry, 2007; Penniston-Dorland and Ferry, 2006). Alternative external sources of reduced fluids would require unidentified processes, including mixing of different carbon reservoirs, or water-rock interactions equivalent to those that took place in the BMC.

A reducing potential internal to the BMC, and in particular the hydroxylation of fresh mantle peridotites during the Taconic subduction, appears the most likely interpretation for the genesis of the identified reduced fluid species. The presence of Fe-Ni alloys in the BMC partially serpentinized peridotites indicates that the rock recorded reducing conditions, as already observed in several oceanic and ophiolitic, and some subduction zone serpentinites (Evans et al., 2017; Frost, 1985; Klein and Bach, 2009; Vitale Brovarone et al., 2020). High-pressure syn-serpentinization reducing conditions are also suggested by the thermodynamic modelling results presented in this study, which indicates fO_2 values as low as $-3.2 \Delta QFM$ at 400 °C and 1 GPa to $-1.2 \Delta QFM$ at 450 °C and 1 GPa, and the formation of significant amounts of H_2 in the fluid (Fig. 10C). The interaction of this H_2 with dissolved carbon, nitrogen, and sulphur species present in the serpentinizing fluid, could have favoured the formation of CH_4 , H_2S , and NH_3 from more oxidized species. For NH_3 , the modelling also indicates that this species is already the dominant N species in the infiltrating fluid buffered at QFM. This feature suggests that the N_2 detected in the fluid is most likely formed through post-entrapment respeciation of NH_3 , unless the serpentinizing fluid was more oxidized than QFM. The absence of detectable H_2O in the fluid inclusions is interpreted to result from host-inclusion interaction and formation of step-daughter lizardite and brucite, or by the preferential entrapment of immiscible reduced gases relative to aqueous fluids (Huang et al., 2017; Vitale Brovarone et al., 2017). The absence of residual H_2 in the fluid inclusions may be explained by the much faster diffusion H_2 relative to other fluid species through the host olivine, or by selective leakage.

The most plausible sources of serpentinizing fluid were the metasedimentary formations surrounding the BMC complex. These rock types host substantial amounts of subducted carbon, sulphur, and nitrogen (Bebout and Fogel, 1992; Evans et al., 2014; Kelemen and

Manning, 2015; Plank and Manning, 2019). An ultramafic source internal to the BMC would not be consistent with the general retention of N during prograde metamorphism and dehydration of serpentinites (Halama et al., 2014). The hypothesis of a metasediment-derived serpentinizing fluid was also suggested by previous oxygen and hydrogen isotopic data on antigorite from the BMC complex (Wenner and Taylor, 1974, 1971). Moreover, the authors proposed antigorite-magnetite equilibration T in the range of 220-460 °C, which is consistent with the prograde P-T of the BMC (Fig. 12). This supports the interpretation of a subduction-related serpentinization related to the infiltration of metasedimentary-derived fluids in a rather dry ultramafic body.

5. Conclusions

Mineralogical, microstructural, and fluid inclusion study of variably serpentinized dunite from the Belvidere Mountain Complex, Appalachian belt, Northern Vermont, provides insight into the process of high-pressure serpentinization in subduction zone and the related fluid-rock redox patterns. Although the BMC underwent a complex tectonic evolution potentially characterized by multiple stages of hydration from the (sub)seafloor to subduction and exhumation, the collected data point to a major event of high-pressure serpentinization that took place in the Appalachian subduction zone. Metamorphic olivine in the BMC serpentinized peridotite is interpreted as the product of rock hydration rather than dehydration, linked to the high-pressure serpentinization event. Our data support the hypothesis that the methane observed in olivine-hosted secondary fluid inclusions is genetically linked to serpentinization in the antigorite stability field consistent with the high-pressure portion of the prograde or retrograde P-T path of the BMC. This favors an abiotic origin for this methane, even though a biotic origin for the C source cannot be excluded. The

C- and N-rich composition of fluid inclusions suggests a metasediment-derived origin for the serpentizing fluid. The high-pressure serpentinization and related abiotic methanogenesis place the Belvidere mountain complex as a suitable proxy for the study of mantle wedge serpentinization. This study confirms the importance of fluid mobility in deep seated ultramafic body in subduction zones for the mobility of C, H, and N, and their implications on large-scale geochemical cycling.

6. Acknowledgments

AVB acknowledges a MIUR Rita Levi Montalcini grant and a Richard Lounsbery Foundation grant. Simona Ferrando is thanked for her helpful discussions and insights on fluid inclusions. IFP Energies Nouvelles and its helpful personnel is thanked for its help in the acquisition on test isotopic data of methane.

7. References

- Andréani, M., Mével, C., Boullier, A.-M., Escartin, J., 2007. Dynamic control on serpentine crystallization in veins: Constraints on hydration processes in oceanic peridotites. *Geochem. Geophys. Geosystems* 8.
- Andreani, M., Munoz, M., Marcaillou, C., Delacour, A., 2013. μ XANES study of iron redox state in serpentine during oceanic serpentinization. *Lithos* 178, 70–83.
- Arai, S., Ishimaru, S., Mizukami, T., 2012. Methane and propane micro-inclusions in olivine in titanoclinohumite-bearing dunites from the Sanbagawa high-P metamorphic belt, Japan: Hydrocarbon activity in a subduction zone and Ti mobility. *Earth Planet. Sci. Lett.* 353, 1–11.
- Auzende, A.-L., Daniel, I., Reynard, B., Lemaire, C., Guyot, F., 2004. High-pressure behaviour of serpentine minerals: a Raman spectroscopic study. *Phys. Chem. Miner.* 31, 269–277.
- Bebout, G.E., Fogel, M.L., 1992. Nitrogen-isotope compositions of metasedimentary rocks in the Catalina Schist, California: implications for metamorphic devolatilization history. *Geochim. Cosmochim. Acta* 56, 2839–2849.
- Bebout, G.E., Penniston-Dorland, S.C., 2016. Fluid and mass transfer at subduction interfaces—The field metamorphic record. *Lithos* 240–243, 228–258.
<https://doi.org/10.1016/j.lithos.2015.10.007>
- Berkesi, M., Hidas, K., Guzmics, T., Dubessy, J., Bodnar, R.J., Szabó, C., Vajna, B., Tsunogae, T., 2009. Detection of small amounts of H₂O in CO₂-rich fluid inclusions using Raman spectroscopy. *J. Raman Spectrosc. Int. J. Orig. Work Asp. Raman Spectrosc. High. Order Process. Also Brillouin Rayleigh Scatt.* 40, 1461–1463.
- Berman, R.G., 1988. Internally-consistent thermodynamic data for minerals in the system Na₂O-K₂O-CaO-MgO-FeO-Fe₂O₃-Al₂O₃-SiO₂-TiO₂-H₂O-CO₂. *J. Petrol.* 29, 445–522.

552 Berndt, M.E., Allen, D.E., Seyfried Jr, W.E., 1996. Reduction of CO₂ during serpentinization of olivine
 553 at 300 C and 500 bar. *Geology* 24, 351–354.
 554 Cannat, M., Fontaine, F., Escartin, J., 2010. Serpentinization and associated hydrogen and methane
 555 fluxes at slow spreading ridges. *Divers. Hydrothermal Syst. Slow Spreading Ocean Ridges*
 556 188, 241–264.
 557 Castonguay, S., Kim, J., Thompson, P.J., Gale, M.H., Joyce, N., Laird, J., Doolan, B.L., 2012. Timing of
 558 tectonometamorphism across the Green Mountain anticlinorium, northern Vermont
 559 Appalachians: 40Ar/39Ar data and correlations with southern Quebec. *GSA Bull.* 124, 352–
 560 367. <https://doi.org/10.1130/B30487.1>
 561 Caumon, M.-C., Tarantola, A., Wang, W., 2019. Raman spectra of gas mixtures in fluid inclusions:
 562 Effect of quartz birefringence on composition measurement. *J. Raman Spectrosc.*
 563 Cesare, B., 1995. Graphite precipitation in C—O—H fluid inclusions: closed system compositional and
 564 density changes, and thermobarometric implications. *Contrib. Mineral. Petrol.* 122, 25–33.
 565 Chew, D.M., van Staal, C.R., 2014. The ocean–continent transition zones along the Appalachian–
 566 Caledonian Margin of Laurentia: Examples of large-scale hyperextension during the opening
 567 of the Iapetus Ocean. *Geosci. Can.* 41, 165–185.
 568 Chidester, A.H., Albee, A.L., Cady, W.M., 1978. Petrology, structure, and genesis of the asbestos-
 569 bearing ultramafic rocks of the Belvidere Mountain area in Vermont. *US Govt. Print. Off.*,
 570 Connolly, J.A.D., 1995. Phase diagram methods for graphitic rocks and application to the system C-
 571 O- H- FeO- TiO₂- SiO₂. *Contrib. Mineral. Petrol.* 119, 94–116.
 572 Dandar, O., Okamoto, A., Uno, M., Oyanagi, R., Nagaya, T., Burenjargal, U., Miyamoto, T., Tsuchiya,
 573 N., 2019. Formation of secondary olivine after orthopyroxene during hydration of mantle
 574 wedge: evidence from the Khantaishir Ophiolite, western Mongolia. *Contrib. Mineral. Petrol.*
 575 174, 86.
 576 Debret, B., Nicollet, C., Andreani, M., Schwartz, S., Godard, M., 2013. Three steps of serpentinization
 577 in an eclogitized oceanic serpentinization front (Lanzo Massif–Western Alps). *J. Metamorph.*
 578 *Geol.* 31, 165–186.
 579 Deschamps, F., Godard, M., Guillot, S., Hattori, K., 2013. Geochemistry of subduction zone
 580 serpentinites: A review. *Lithos* 178, 96–127.
 581 Doolan, B.L., Gale, M.H., Gale, P.N., Hoar, R.S., St-Julien, P., 1982. Geology of the Quebec re-entrant:
 582 possible constraints from early rifts and the Vermont-Quebec serpentine belt. *Major Struct.*
 583 *Zones Faults North. Appalach. Ed. P St-Julien J Béland Geol. Assoc. Can. Spec. Pap.* 24, 87–
 584 115.
 585 Etiope, G., Schoell, M., Hosgörmez, H., 2011. Abiotic methane flux from the Chimaera seep and
 586 Tekirova ophiolites (Turkey): understanding gas exhalation from low temperature
 587 serpentinization and implications for Mars. *Earth Planet. Sci. Lett.* 310, 96–104.
 588 Etiope, G., Sherwood Lollar, B., 2013. Abiotic methane on Earth. *Rev. Geophys.* 51, 276–299.
 589 Evans, B.W., 2010. Lizardite versus antigorite serpentine: Magnetite, hydrogen, and life (?).
 590 *Geology* 38, 879–882.
 591 Evans, B.W., 2008. Control of the products of serpentinization by the Fe²⁺/Mg-1 exchange potential
 592 of olivine and orthopyroxene. *J. Petrol.* 49, 1873–1887.
 593 Evans, B.W., 2004. The serpentine multisystem revisited: chrysotile is metastable. *Int. Geol. Rev.*
 594 46, 479–506.
 595 Evans, K.A., Bickle, M.J., Skelton, A.D.L., Hall, M., Chapman, H., 2002. Reductive deposition of
 596 graphite at lithological margins in East Central Vermont: a Sr, C and O isotope study. *J.*
 597 *Metamorph. Geol.* 20, 781–798.
 598 Evans, K.A., Reddy, S.M., Tomkins, A.G., Crossley, R.J., Frost, B.R., 2017. Effects of geodynamic
 599 setting on the redox state of fluids released by subducted mantle lithosphere. *Lithos* 278–
 600 281, 26–42. <https://doi.org/10.1016/j.lithos.2016.12.023>
 601 Evans, K.A., Tomkins, A.G., Cliff, J., Fiorentini, M.L., 2014. Insights into subduction zone sulfur
 602 recycling from isotopic analysis of eclogite-hosted sulfides. *Chem. Geol.* 365, 1–19.

- Ferry, J.M., 2007. The role of volatile transport by diffusion and dispersion in driving biotite-forming reactions during regional metamorphism of the Gile Mountain Formation, Vermont. *Am. Mineral.* 92, 1288–1302.
- Frezzotti, M.L., Tecce, F., Casagli, A., 2012. Raman spectroscopy for fluid inclusion analysis. *J. Geochem. Explor.* 112, 1–20.
- Frost, B.R., 1985. On the stability of sulfides, oxides, and native metals in serpentinite. *J. Petrol.* 26, 31–63.
- Frost, B.R., Beard, J.S., 2007. On silica activity and serpentinization. *J. Petrol.* 48, 1351–1368.
- Früh-Green, G.L., Connolly, J.A., Plas, A., Kelley, D.S., Grobéty, B., 2004. Serpentinization of oceanic peridotites: implications for geochemical cycles and biological activity. *Subseafloor Biosphere -Ocean Ridges* 144, 119–136.
- Gale, M.H., 2007. Bedrock Geologic Map of the Hazens Notch and Portions of the Eden and Lowell Quadrangles, Vermont. *Vt. Geol. Surv., Vermont geological open file report VG07-2, plate 1.*
- Gale, M.H., 1986. Geologic map of the Belvidere Mountain area, Eden and Lowell, Vermont (USGS Numbered Series No. 1560), IMAP.
- Gale, M.H., 1980. Geology of the Belvidere Mountain Complex, Eden and Lowell, Vermont. US Geological Survey,.
- Grozeva, N.G., Klein, F., Seewald, J.S., Sylva, S.P., 2020. Chemical and isotopic analyses of hydrocarbon-bearing fluid inclusions in olivine-rich rocks. *Philos. Trans. R. Soc. A* 378, 20180431.
- Guillot, S., Hattori, K.H., de Sigoyer, J., 2000. Mantle wedge serpentinization and exhumation of eclogites: insights from eastern Ladakh, northwest Himalaya. *Geology* 28, 199–202.
- Guillot, S., Schwartz, S., Reynard, B., Agard, P., Prigent, C., 2015. Tectonic significance of serpentinites. *Tectonophysics* 646, 1–19.
- Halama, R., Bebout, G.E., John, T., Scambelluri, M., 2014. Nitrogen recycling in subducted mantle rocks and implications for the global nitrogen cycle. *Int. J. Earth Sci.* 103, 2081–2099.
- Hibbard, J.P., Van Staal, C.R., Rankin, D.W., Williams, H., 2006. Lithotectonic map of the Appalachian orogen, Canada–United States of America. *Geol. Surv. Can. Map A* 2096, 2.
- Holloway, J.R., 1984. Graphite-CH₄-H₂O-CO₂ equilibria at low-grade metamorphic conditions. *Geology* 12, 455–458.
- Holm, N.G., Charlou, J.L., 2001. Initial indications of abiogenic formation of hydrocarbons in the Rainbow ultramafic hydrothermal system, Mid-Atlantic Ridge. *Earth Planet. Sci. Lett.* 191, 1–8.
- Honsberger, I.W., 2015. Metamorphism, deformation, geochemistry, and tectonics of exhumed ultramafic and mafic rocks in the central and north-central Vermont Appalachians.
- Honsberger, I.W., Laird, J., Thompson, P.J., 2017. A tectonized ultramafic-mafic-pelitic package in Stockbridge, Vermont: Metamorphism resulting from subduction and exhumation. *Am. J. Sci.* 317, 1019–1047.
- Huang, F., Daniel, I., Cardon, H., Montagnac, G., Sverjensky, D.A., 2017. Immiscible hydrocarbon fluids in the deep carbon cycle. *Nat. Commun.* 8, 1–8.
- Iyer, K., Austrheim, H., John, T., Jamtveit, B., 2008. Serpentinization of the oceanic lithosphere and some geochemical consequences: constraints from the Leka Ophiolite Complex, Norway. *Chem. Geol.* 249, 66–90.
- Karabinos, P., Samson, S.D., Hepburn, J.C., Stoll, H.M., 1998. Taconian orogeny in the New England Appalachians: Collision between Laurentia and the Shelburne Falls arc. *Geology* 26, 215–218. [https://doi.org/10.1130/0091-7613\(1998\)026<0215:TOITNE>2.3.CO;2](https://doi.org/10.1130/0091-7613(1998)026<0215:TOITNE>2.3.CO;2)
- Kelemen, P.B., Manning, C.E., 2015. Reevaluating carbon fluxes in subduction zones, what goes down, mostly comes up. *Proc. Natl. Acad. Sci.* 112, E3997–E4006. <https://doi.org/10.1073/pnas.1507889112>
- Kelley, D.S., Karson, J.A., Früh-Green, G.L., Yoerger, D.R., Shank, T.M., Butterfield, D.A., Hayes, J.M., Schrenk, M.O., Olson, E.J., Proskurowski, G., Jakuba, M., Bradley, A., Larson, B., Ludwig, K.,

- Glickson, D., Buckman, K., Bradley, A.S., Brazelton, W.J., Roe, K., Elend, M.J., Delacour, A., Bernasconi, S.M., Lilley, M.D., Baross, J.A., Summons, R.E., Sylva, S.P., 2005. A Serpentinite-Hosted Ecosystem: The Lost City Hydrothermal Field. *Science* 307, 1428–1434. <https://doi.org/10.1126/science.1102556>
- Kempf, E.D., Hermann, J., 2018. Hydrogen incorporation and retention in metamorphic olivine during subduction: Implications for the deep water cycle. *Geology* 46, 571–574.
- Klein, F., Bach, W., 2009. Fe–Ni–Co–O–S phase relations in peridotite–seawater interactions. *J. Petrol.* 50, 37–59.
- Klein, F., Bach, W., Humphris, S.E., Kahl, W.-A., Jöns, N., Moskowicz, B., Berquó, T.S., 2014. Magnetite in seafloor serpentinite—Some like it hot. *Geology* 42, 135–138.
- Klein, F., Bach, W., McCollom, T.M., 2013. Compositional controls on hydrogen generation during serpentinization of ultramafic rocks. *Lithos* 178, 55–69.
- Klein, F., Grozeva, N.G., Seewald, J.S., 2019. Abiotic methane synthesis and serpentinization in olivine-hosted fluid inclusions. *Proc. Natl. Acad. Sci.* 116, 17666–17672.
- Laird, J., Lanphere, M.A., Albee, A.L., 1984. Distribution of Ordovician and Devonian metamorphism in mafic and pelitic schists from northern Vermont. *Am. J. Sci.* 284, 376–413.
- Laird, J., Trzcinski, W.E., Bothner, W.A., Cheney, J.T., Hepburn, J.C., 1993. High-pressure, Taconian, and subsequent polymetamorphism of southern Quebec and northern Vermont. *Contrib. Dep. Univ. Mass.* 67, 1–32.
- Lamadrid, H.M., Rimstidt, J.D., Schwarzenbach, E.M., Klein, F., Ulrich, S., Dolocan, A., Bodnar, R.J., 2017. Effect of water activity on rates of serpentinization of olivine. *Nat. Commun.* 8, 1–9.
- Li, L., Cartigny, P., Ader, M., 2009. Kinetic nitrogen isotope fractionation associated with thermal decomposition of NH₃: Experimental results and potential applications to trace the origin of N₂ in natural gas and hydrothermal systems. *Geochim. Cosmochim. Acta* 73, 6282–6297.
- Majumdar, A.S., Hövelmann, J., Vollmer, C., Berndt, J., Mondal, S.K., Putnis, A., 2016. Formation of Mg-rich olivine pseudomorphs in serpentinized dunite from the Mesoarchean Nuasahi Massif, Eastern India: Insights into the evolution of fluid composition at the mineral–fluid interface. *J. Petrol.* 57, 3–26.
- McCollom, T.M., 2016. Abiotic methane formation during experimental serpentinization of olivine. *Proc. Natl. Acad. Sci.* 113, 13965–13970.
- Ménez, B., Pisapia, C., Andreani, M., Jamme, F., Vanbellingen, Q.P., Brunelle, A., Richard, L., Dumas, P., Réfrégiers, M., 2018. Abiotic synthesis of amino acids in the recesses of the oceanic lithosphere. *Nature* 564, 59–63. <https://doi.org/10.1038/s41586-018-0684-z>
- Mével, C., 2003. Serpentinization of abyssal peridotites at mid-ocean ridges. *Comptes Rendus Geosci.* 335, 825–852.
- Moody, J.B., 1976. Serpentinization: a review. *Lithos* 9, 125–138.
- Nozaka, T., 2018. Compositional variation of olivine related to high-temperature serpentinization of peridotites: Evidence from the Oeyama ophiolite. *J. Mineral. Petrol. Sci.* 180420.
- Nozaka, T., 2003. Compositional heterogeneity of olivine in thermally metamorphosed serpentinite from Southwest Japan. *Am. Mineral.* 88, 1377–1384.
- Penniston-Dorland, S.C., Ferry, J.M., 2006. Development of spatial variations in reaction progress during regional metamorphism of micaceous carbonate rocks, northern New England. *Am. J. Sci.* 306, 475–524.
- Plank, T., Manning, C.E., 2019. Subducting carbon. *Nature* 574, 343–352.
- Plümper, O., John, T., Podladchikov, Y.Y., Vrijmoed, J.C., Scambelluri, M., 2017. Fluid escape from subduction zones controlled by channel-forming reactive porosity. *Nat. Geosci.* 10, 150–156. <https://doi.org/10.1038/ngeo2865>
- Plümper, O., King, H.E., Vollmer, C., Ramasse, Q., Jung, H., Austrheim, H., 2012a. The legacy of crystal-plastic deformation in olivine: high-diffusivity pathways during serpentinization. *Contrib. Mineral. Petrol.* 163, 701–724.

- Plümper, O., Piazzolo, S., Austrheim, H., 2012b. Olivine pseudomorphs after serpentinized orthopyroxene record transient oceanic lithospheric mantle dehydration (Leka Ophiolite Complex, Norway). *J. Petrol.* 53, 1943–1968.
- Rouméjon, S., Andreani, M., Früh-Green, G.L., 2019. Antigorite crystallization during oceanic retrograde serpentinization of abyssal peridotites. *Contrib. Mineral. Petrol.* 174, 60.
- Rumble III, D., Hoering, T.C., 1986. Carbon isotope geochemistry of graphite vein deposits from New Hampshire, USA. *Geochim. Cosmochim. Acta* 50, 1239–1247.
- Scambelluri, M., Müntener, O., Hermann, J., Piccardo, G.B., Trommsdorff, V., 1995. Subduction of water into the mantle: history of an Alpine peridotite. *Geology* 23, 459–462.
- Scambelluri, M., Strating, E.H., Piccardo, G.B., Vissers, R.L.M., Rampone, E., 1991. Alpine olivine-and titanite clinohumite-bearing assemblages in the Erro-Tobbio peridotite (Voltri Massif, NW Italy). *J. Metamorph. Geol.* 9, 79–91.
- Scambelluri, M., Tonarini, S., 2012. Boron isotope evidence for shallow fluid transfer across subduction zones by serpentinized mantle. *Geology* 40, 907–910.
- Schrenk, M.O., Brazelton, W.J., Lang, S.Q., 2013. Serpentinization, carbon, and deep life. *Rev. Mineral. Geochem.* 75, 575–606.
- Schwartz, S., Guillot, S., Reynard, B., Lafay, R., Debret, B., Nicollet, C., Lanari, P., Auzende, A.L., 2013. Pressure–temperature estimates of the lizardite/antigorite transition in high pressure serpentinites. *Lithos* 178, 197–210.
- Seyfried Jr, W.E., Foustoukos, D.I., Fu, Q., 2007. Redox evolution and mass transfer during serpentinization: An experimental and theoretical study at 200 C, 500 bar with implications for ultramafic-hosted hydrothermal systems at Mid-Ocean Ridges. *Geochim. Cosmochim. Acta* 71, 3872–3886.
- Shen, T., Hermann, J., Zhang, L., Lü, Z., Padrón-Navarta, J.A., Xia, B., Bader, T., 2015. UHP metamorphism documented in Ti-chondrodite-and Ti-clinohumite-bearing serpentinized ultramafic rocks from Chinese southwestern Tianshan. *J. Petrol.* 56, 1425–1458.
- Sleep, N.H., Bird, D.K., 2007. Niches of the pre-photosynthetic biosphere and geologic preservation of Earth’s earliest ecology. *Geobiology* 5, 101–117.
- Stanley, R.S., Roy, D.L., Hatch, N.L., Knapp, D.A., 1984. Evidence for tectonic emplacement of ultramafic and associated rocks in the pre-Silurian eugeoclinal belt of western New England; vestiges of an ancient accretionary wedge. *Am. J. Sci.* 284, 559–595.
<https://doi.org/10.2475/ajs.284.4-5.559>
- Sverjensky, D.A., Harrison, B., Azzolini, D., 2014. Water in the deep Earth: the dielectric constant and the solubilities of quartz and corundum to 60 kb and 1200 C. *Geochim. Cosmochim. Acta* 129, 125–145.
- Touret, J.L.R., 2001. Fluids in metamorphic rocks. *Lithos* 55, 1–25.
- Trommsdorff, V., Evans, B.W., 1974. Alpine metamorphism of peridotitic rocks. *Schweiz Min Pet Mitt* 54, 333–352.
- Van Baalen, M.R., Mossman, B.T., Gunter, M.E., Francis, C.A., 2009. Environmental Geology of Belvidere Mt.
- Vitale Brovarone, A., Martinez, I., Elmaleh, A., Compagnoni, R., Chaduteau, C., Ferraris, C., Esteve, I., 2017. Massive production of abiotic methane during subduction evidenced in metamorphosed ophicarbonates from the Italian Alps. *Nat. Commun.* 8, 14134.
- Vitale Brovarone, A., Sverjensky, D.A., Piccoli, F., Ressico, F., Giovannelli, D., Daniel, I., 2020. Subduction hides high-pressure sources of energy that may feed the deep subsurface biosphere. *Nat. Commun.* 11, 1–11.
- Viti, C., Mellini, M., Rumori, C., 2005. Exsolution and hydration of pyroxenes from partially serpentinized harzburgites. *Mineral. Mag.* 69, 491–507.
- Wada, I., Wang, K., He, J., Hyndman, R.D., 2008. Weakening of the subduction interface and its effects on surface heat flow, slab dehydration, and mantle wedge serpentinization. *J. Geophys. Res. Solid Earth* 113.

755 Wenner, D.B., Taylor, H.P., 1974. D/H and O18/O16 studies of serpentinization of ultramafic rocks.
756 Geochim. Cosmochim. Acta 38, 1255–1286.
757 Wenner, D.B., Taylor, H.P., 1971. Temperatures of serpentinization of ultramafic rocks based on O
758 18/O 16 fractionation between coexisting serpentine and magnetite. Contrib. Mineral.
759 Petrol. 32, 165–185.
760 Wolery, Tj., Jarek, R.L., 2003. Software user's manual: EQ3/6, version 8.0. Softw. Doc. 8–0.
761 Zhang, S., Ague, J.J., Vitale Brovarone, A., 2018. Degassing of organic carbon during regional
762 metamorphism of pelites, Wepawaug Schist, Connecticut, USA. Chem. Geol. 490, 30–44.
763 <https://doi.org/10.1016/j.chemgeo.2018.05.003>
764

Fig. 1: A: Simplified geological map of Vermont, modified from Hibbard et al., (2006). B: Simplified bedrock geologic map of the Belvidere Mountain Complex and the surrounding formations. Modified after Hibbard et al., (2006). Units description from Hibbard et al., (2006) and Gale, (2007).

Fig. 2: A-B: Photographs of the Belvidere serpentized peridotite in outcrop. C: Weakly serpentized dunite (samples V18-2a and V18-2b). D: Serpentized dunite, with boudinaged meta-gabbro (samples V18-3a and V18-3b).

Fig. 3: A: Photomicrograph of a partially serpentized dunite. B: Partial replacement of primary chromian spinel by magnetite and chlorite. C: Partial replacement of olivine by antigorite. D: Inferred primary orthopyroxene being pseudomorphically replaced by metamorphic olivine. See also Figure 5B. E: Photomicrograph of a pyroxenite layer included in the Belvidere peridotite. The photomicrograph shows radial diopside aggregate pseudomorphic on primary clinopyroxene. Partially serpentized olivine is also visible. F: Magnetite-rich diopside pseudomorphosis on primary clinopyroxene. Note the growth of metamorphic olivine at the rim of the clinopyroxene site. See Figure 5A for SEM-based backscattered electron image. G: Metamorphic diopside replacing primary clinopyroxene. In this case, note the growth of metamorphic olivine along fractures cutting the pseudomorphosis. See Figure 5F for SEM-based backscattered electron image. H: Relict of metamorphic olivine pseudomorphic on primary clinopyroxene. The metamorphic olivine is then partially replaced by serpentine + brucite + magnetite. A-D: Sample V18-2b, E-G: Sample V18-3a; H: sample V18-B3. P-Ol: primary olivine, M-Ol: metamorphic olivine, Atg: antigorite, Chl: chlorite, Mgt: magnetite, Di: diopside, Chr: chromite, Br: brucite, Ctl: chrysotile.

Fig. 4: Raman spectra of solid phases. A: Primary olivine. B Antigorite overgrowing primary olivine. C: Antigorite core (Atg1) and rim (Atg2) (see Fig. 5A). D: Brucite.

Fig. 5: SEM-BSE images of samples V18-2b, V18-3a and V18-B3. A: Microstructural patterns of serpentinization. Two generations of serpentine can be observed based on the BSE contrast, a bright core (Atg1) and a dark rim (Atg2). Note also the striped zonation of primary olivine and the formation of metamorphic olivine. B: Replacement of an inferred primary orthopyroxene crystal by metamorphic olivine. The close-up shows the preservation of clinopyroxene relicts interpreted as exsolutions inside the former orthopyroxene. C: Formation of at the expense of metamorphic. D: Composite aggregate of Fe-Ni and Fe-Cu-Ni alloys and Ni sulphide. E: Growth of metamorphic olivine around a diopside-rich primary clinopyroxene pseudomorphosis. A primary chromina spinel partially converted into magnetite can also be observed. F: Metamorphic diopside replacing primary clinopyroxene. Note the presence of antigorite + metamorphic olivine \pm magnetite along the fractures. In this case, metamorphic olivine occupies the centre of the fractures and is not in contact with diopside, whereas the metamorphic olivine rimming the primary clinopyroxene site is in contact with it. G: Metamorphic olivine growing at the expense of metamorphic diopside (former primary clinopyroxene). The microstructure suggests the former presence of serpentine needles replacing the clinopyroxene and successively replaced by metamorphic olivine. Both Atg1 and Atg2 antigorite generations are present. H: Relict of metamorphic olivine formed at the expense of a primary orthopyroxene site in V18-3b. The metamorphic olivine is partially converted into brucite + serpentine. P-Ol: primary olivine M-Ol: metamorphic olivine Px: pyroxene Di: diopside Mtg: magnetite Chr: chromite Atg: antigorite Br: brucite Ctl: chrysotile NiFeS: nickel and iron sulphite. The presence of antigorite was confirmed by Raman spectroscopy.

Fig. 6: Mg# versus MnO (wt%) diagram showing the compositional variation of primary and metamorphic olivine. The Mn-richest cluster of metamorphic olivine belongs to sample V18-B3 (fully serpentinized peridotite). Background data from Arai et al., (2012); Dandar et al., (2019); Debret et al., (2013); Iyer et al., (2008); Nozaka, (2018); Plümper et al., (2012b); Scambelluri et al., (1995); Shen et al., (2015).

Fig. 7: Photomicrographs of methane-rich fluid inclusion trails in olivine from sample V18-2a. Black arrows indicate fluid inclusion trails. A: Inclusion trail being cut by antigorite veinlets. B: Inclusion trail limited by antigorite veins. C: Secondary trail of fluid inclusions propagating from an antigorite veinlet. D: Photomicrograph showing a fluid-inclusion-rich olivine aggregate. E: Close up of the methane-rich fluid inclusions. F: Close up of a graphite bearing fluid inclusion (red arrow), as confirmed by Raman spectroscopy in (Fig. 8B).

Fig. 8: Raman spectra of fluid inclusions and step-daughter solid phases. A: Inclusion showing a marked CH₄ band and minor peaks of N₂, NH₃ and S-H bond. Lizardite and brucite O-H bands are also observed. B: Graphite in fluid inclusions (see Fig. 6D). C: Methane-rich fluid inclusion with a close up of O-H bonds of lizardite and brucite.

Fig. 9: Calculated molar fraction of CH₄, N₂, H₂S and NH₃ from Raman scattering cross-section and the instrumental efficiency of each species. See Frezzotti et al., (2012) for methodology.

Fig. 10: Thermodynamic modelling of HP serpentinization of dunite and related mineralogical and fluid evolution. A: Mineralogical evolution during serpentinization at 450 °C and 1 GPa. Representative microstructures of the main reaction steps are proposed as observed in the natural samples. B: Evolution of the nitrogen and sulphur fluid speciation as a function of the reaction progress presented in A. C: Evolution of the fO₂ and H₂, CH₄, and CO₂ concentrations in the fluid as a function of the reaction progress presented in A.

70 **Fig. 11:** Reconstruction of the mineralogical evolution of the BMC partially serpentized
71 peridotite. An early step of serpentization is proposed based on the needle-like growth of
72 metamorphic olivine on primary clinopyroxene, suggesting the presence of serpentine prior to
73 the formation of metamorphic olivine. The successive growth of antigorite at the expense of
74 both primary and metamorphic olivine constrains the main serpentization event to
75 metamorphic conditions. Finally, a late serpentization event is proposed based on the
76 growth of brucite + antigorite + chrysotile on relict metamorphic. Chr : chromite, P-Ol : primary
77 olivine, M-Ol : metamorphic olivine, Opx : primary orthopyroxene, Cpx : primary clinopyroxene,
78 Chl : chlorite, Mgt : magnetite, Atg : antigorite, Di : diopside, Brc : brucite, Ctl : chrysotile.

79 **Fig. 12:** Stability field of serpentine type minerals and olivine, modified from Guillot et al.,
80 (2015) (see references therein for details on the main reactions). The retrograde P-T path of
81 BMC from Honsberger, (2015) is also shown for reference. Atg : antigorite, Brc : brucite; Ctl :
82 chrysotile; Ilm : ilmenite; Ol : olivine; Tlc : talc; Ticl : titanian clinohumite.

Figure 1

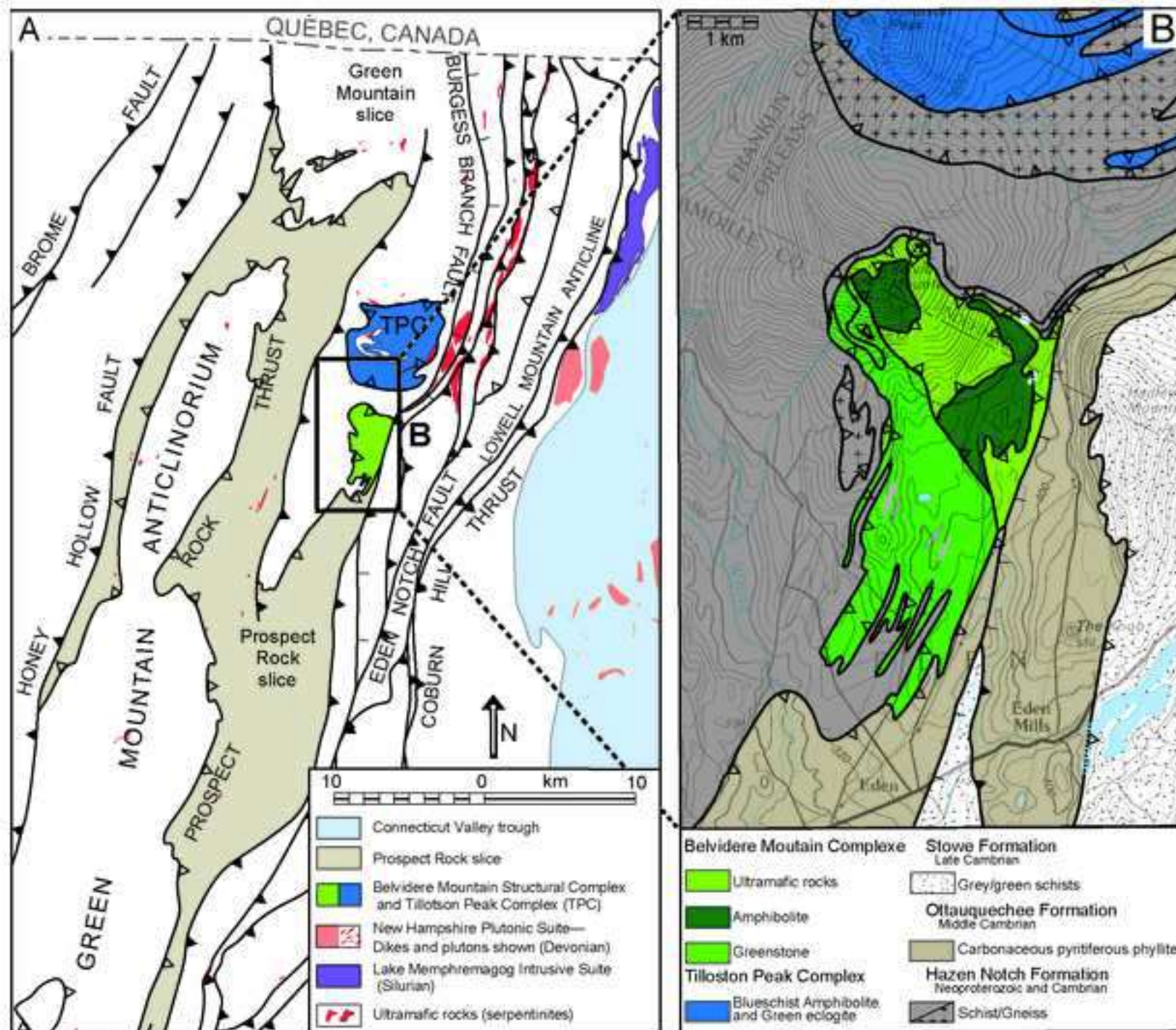


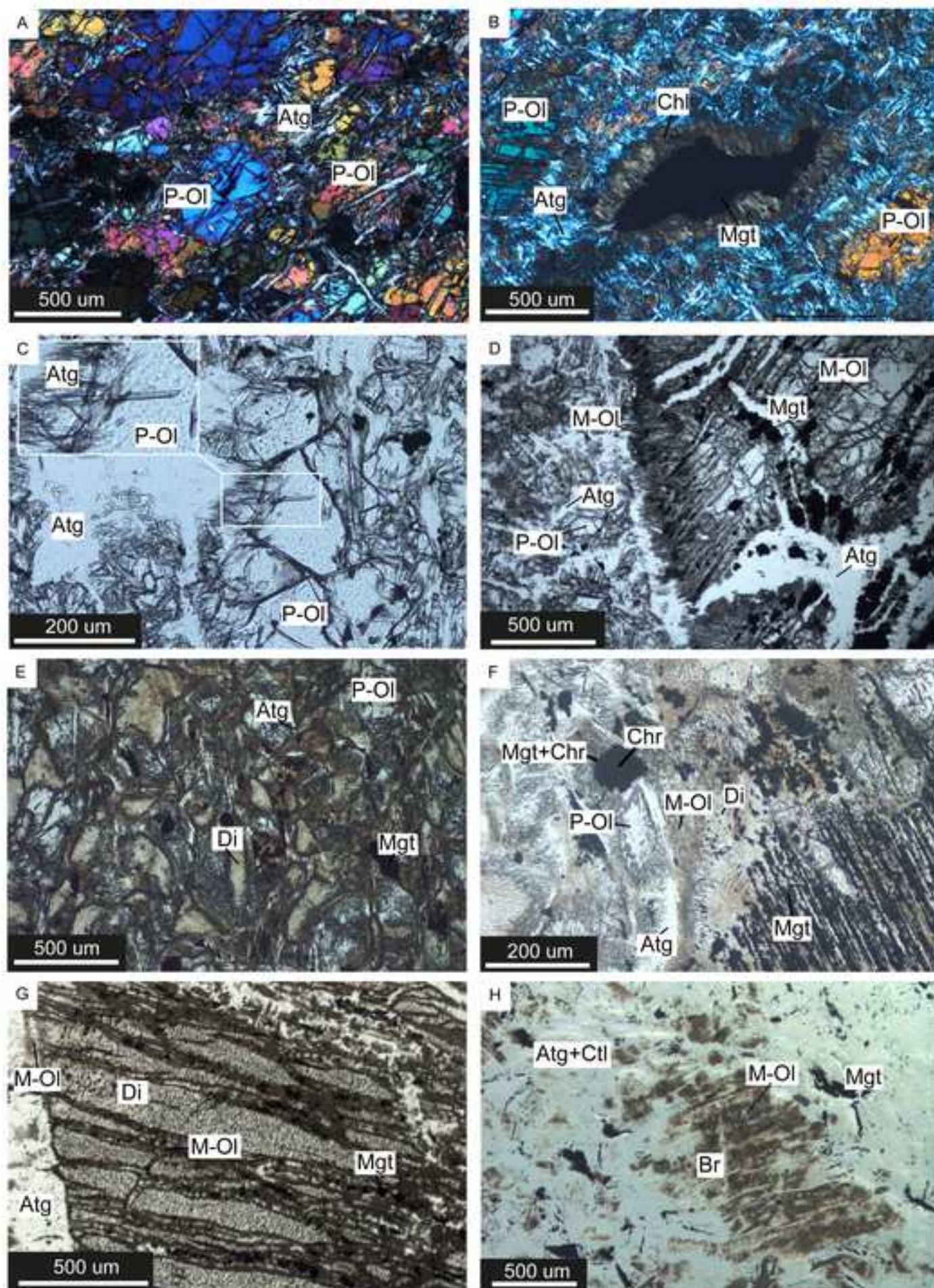
Figure 2

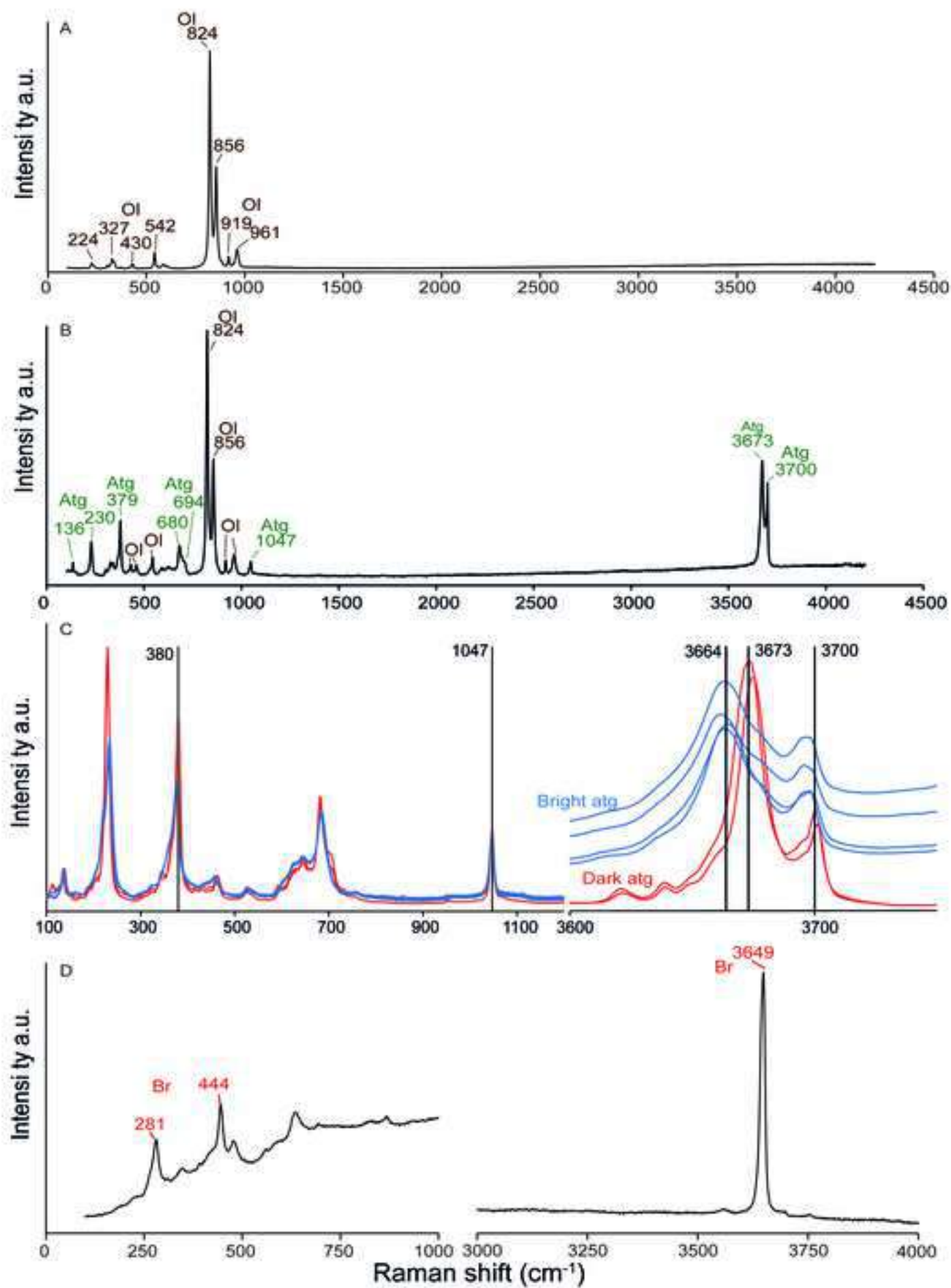
[Click here to access/download;Figure;Fig2.tif](#)

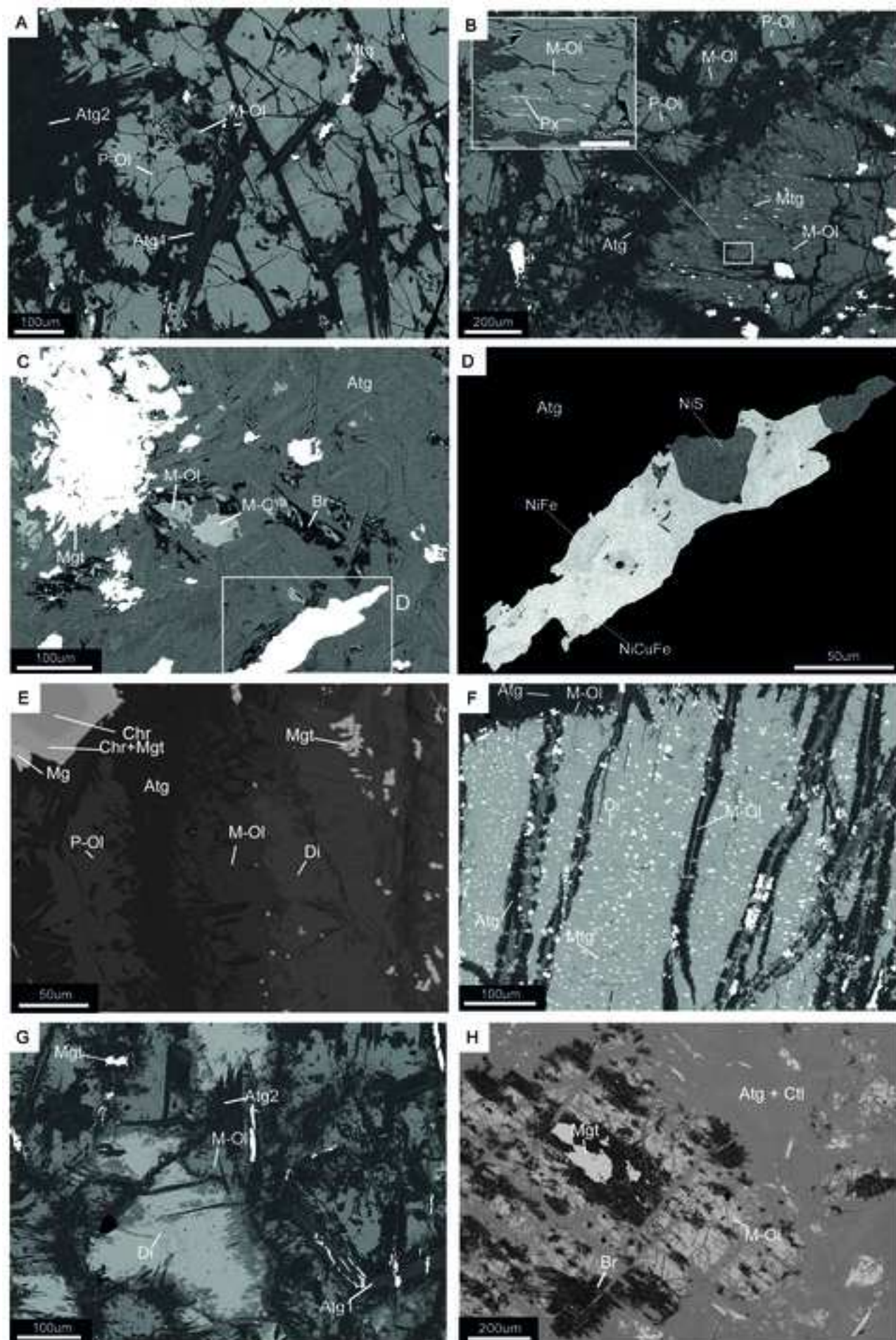


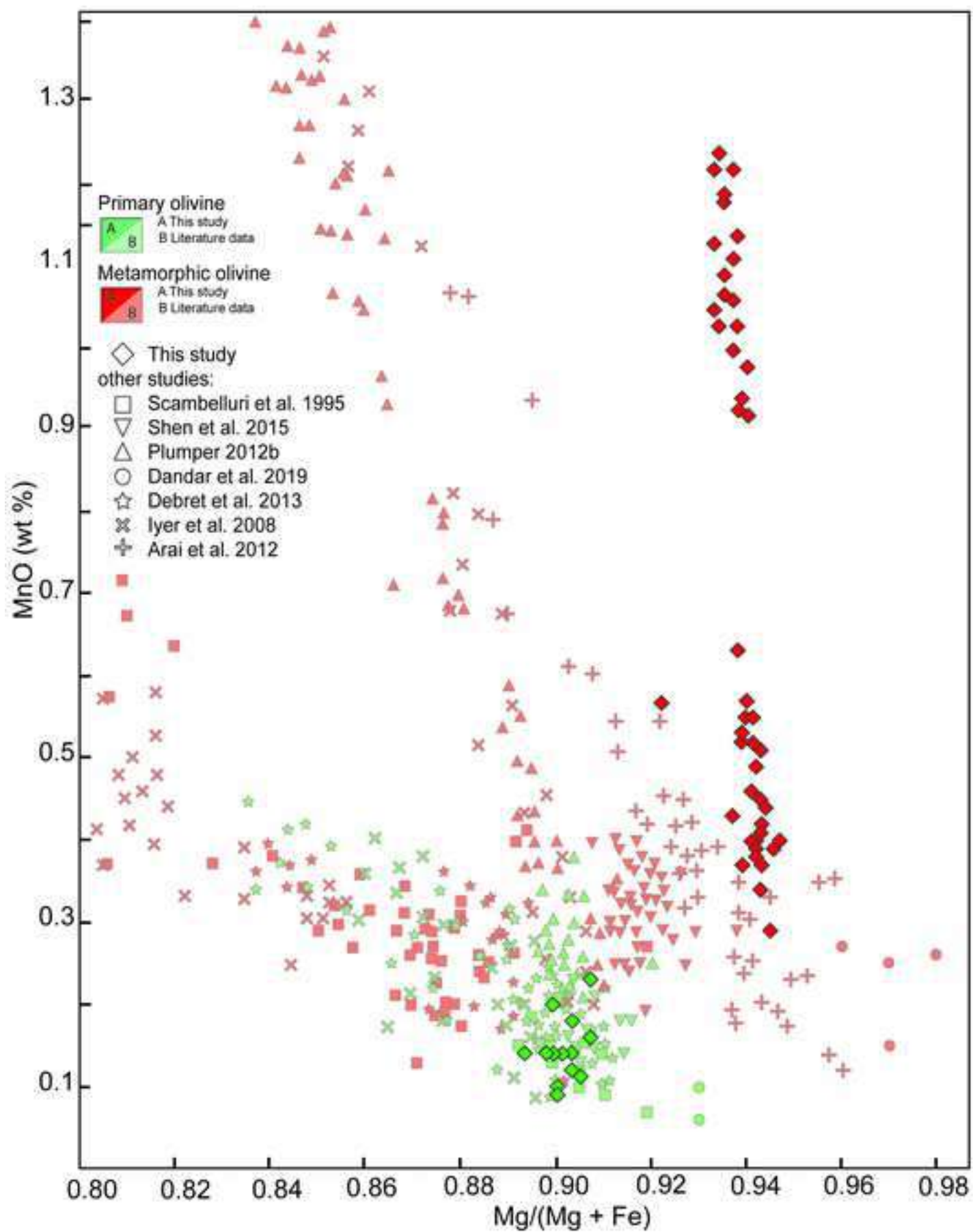
Figure 3

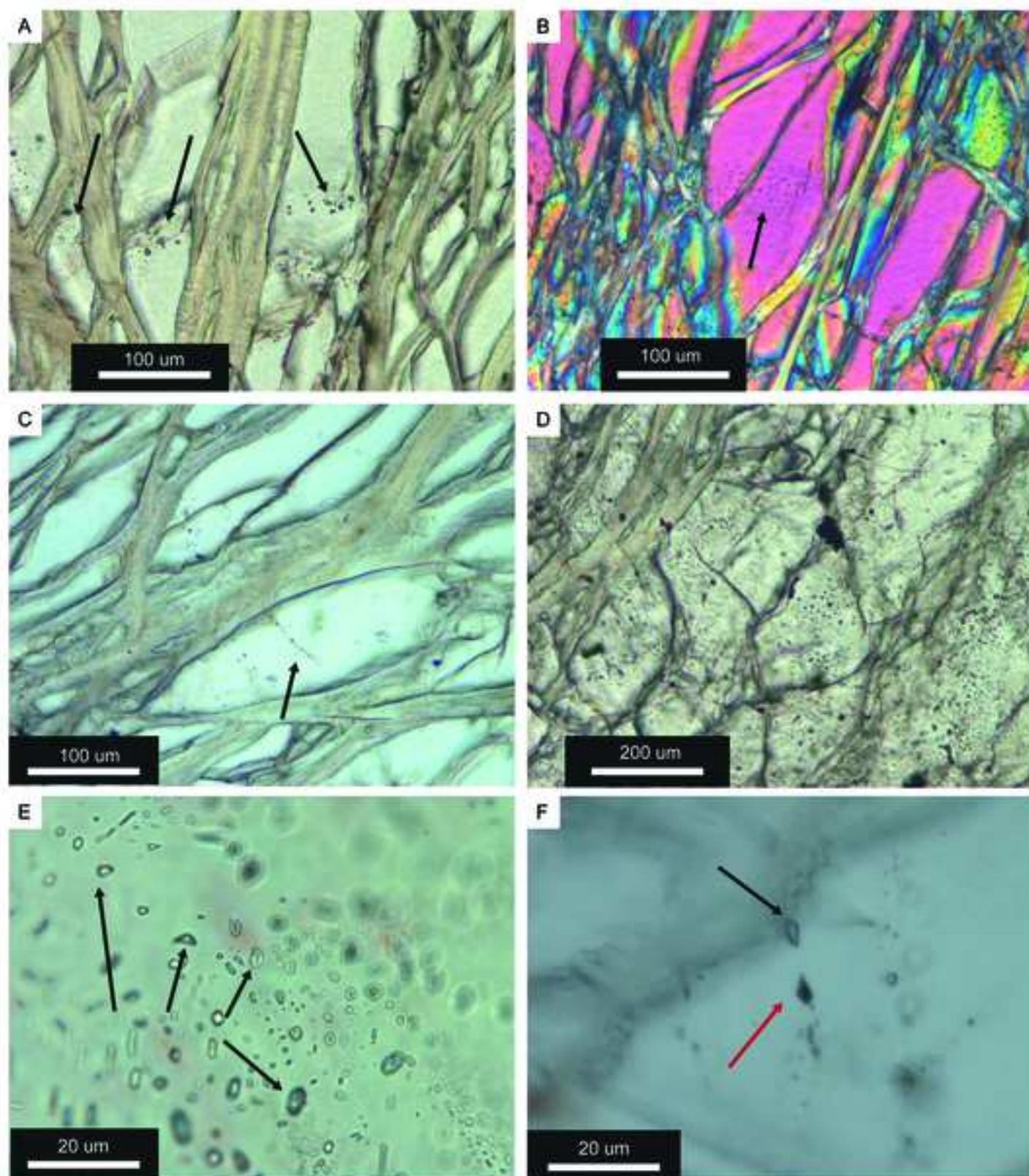
[Click here to access/download;Figure;Fig3.tif](#)











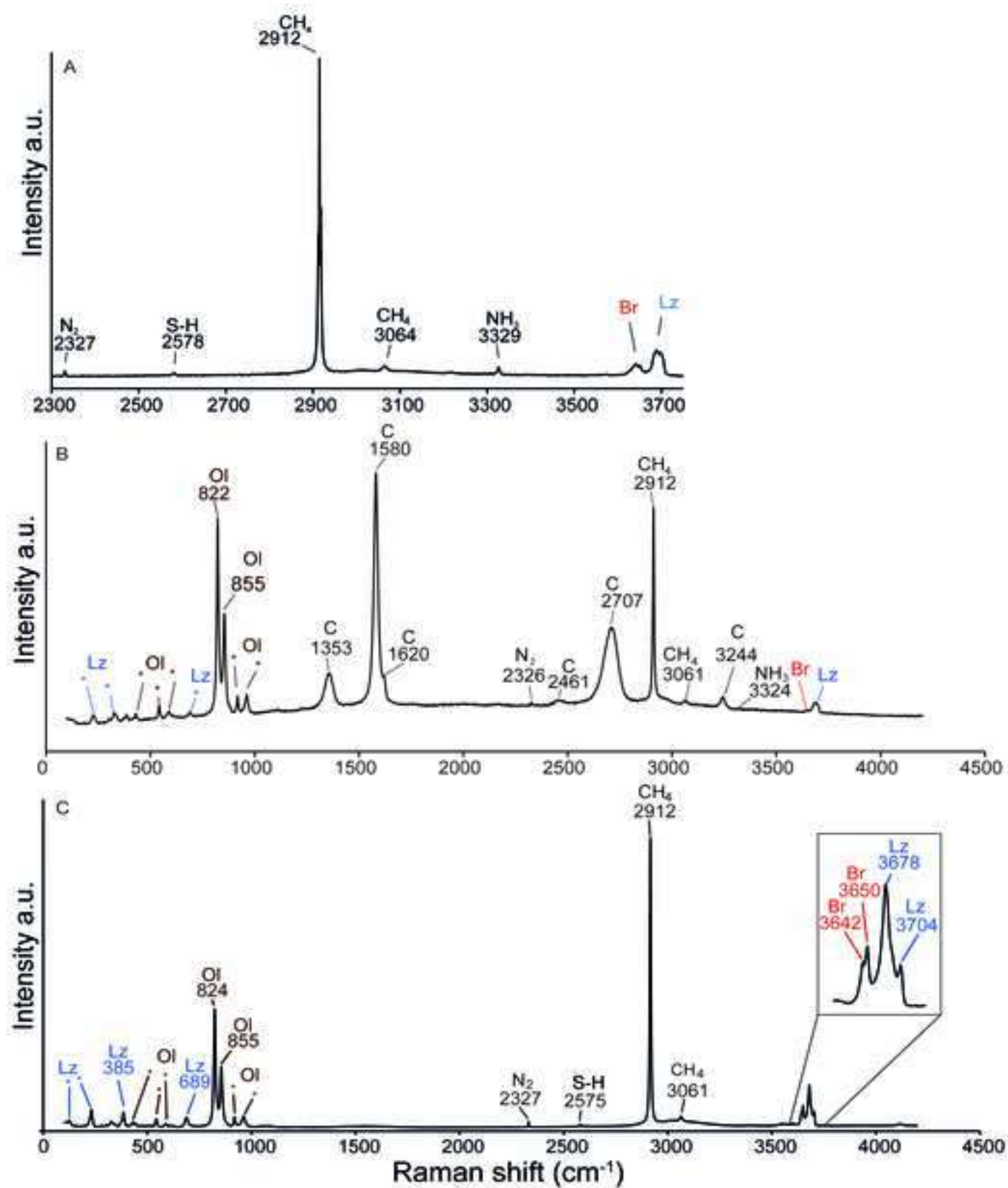


Figure 9

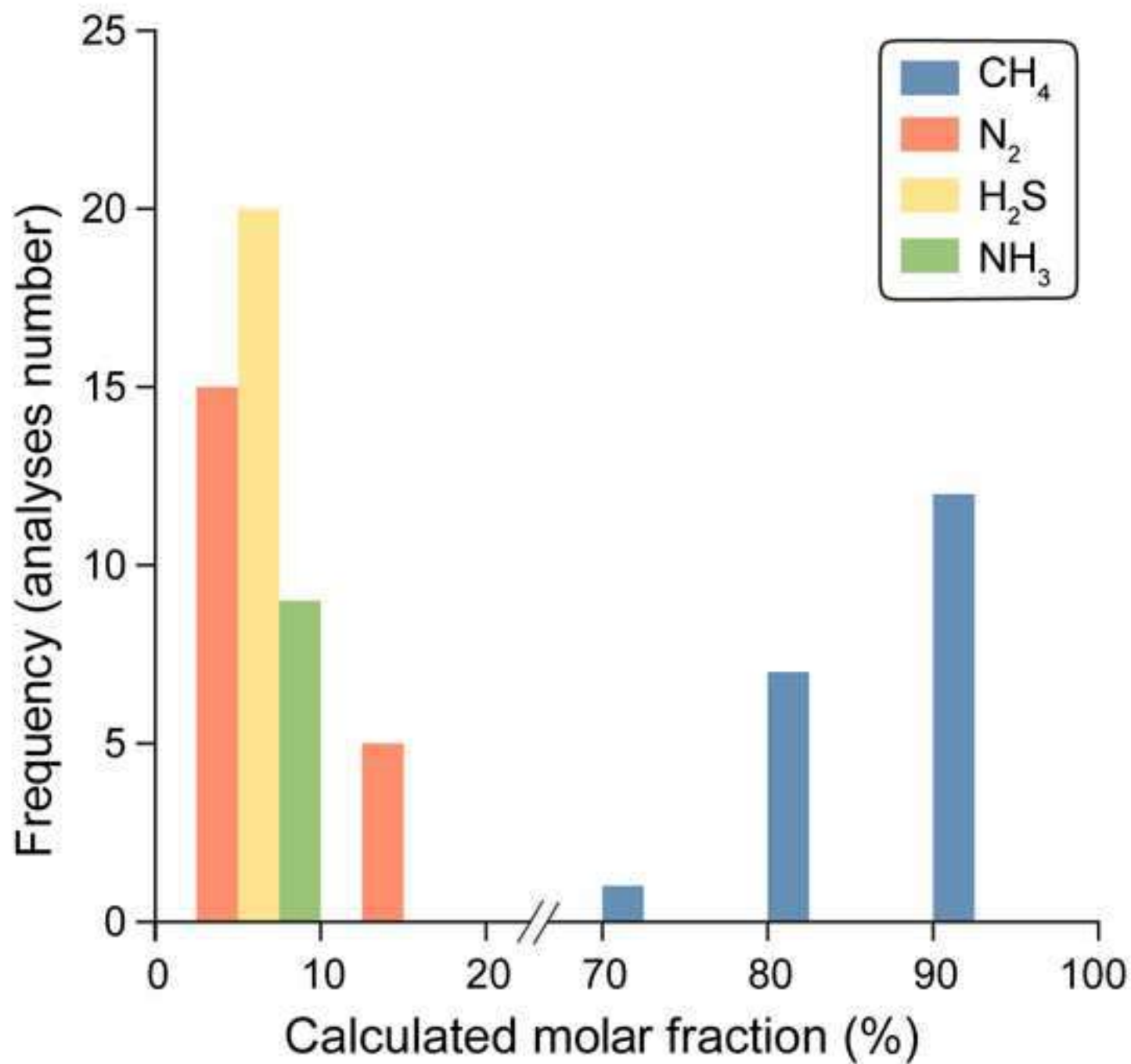
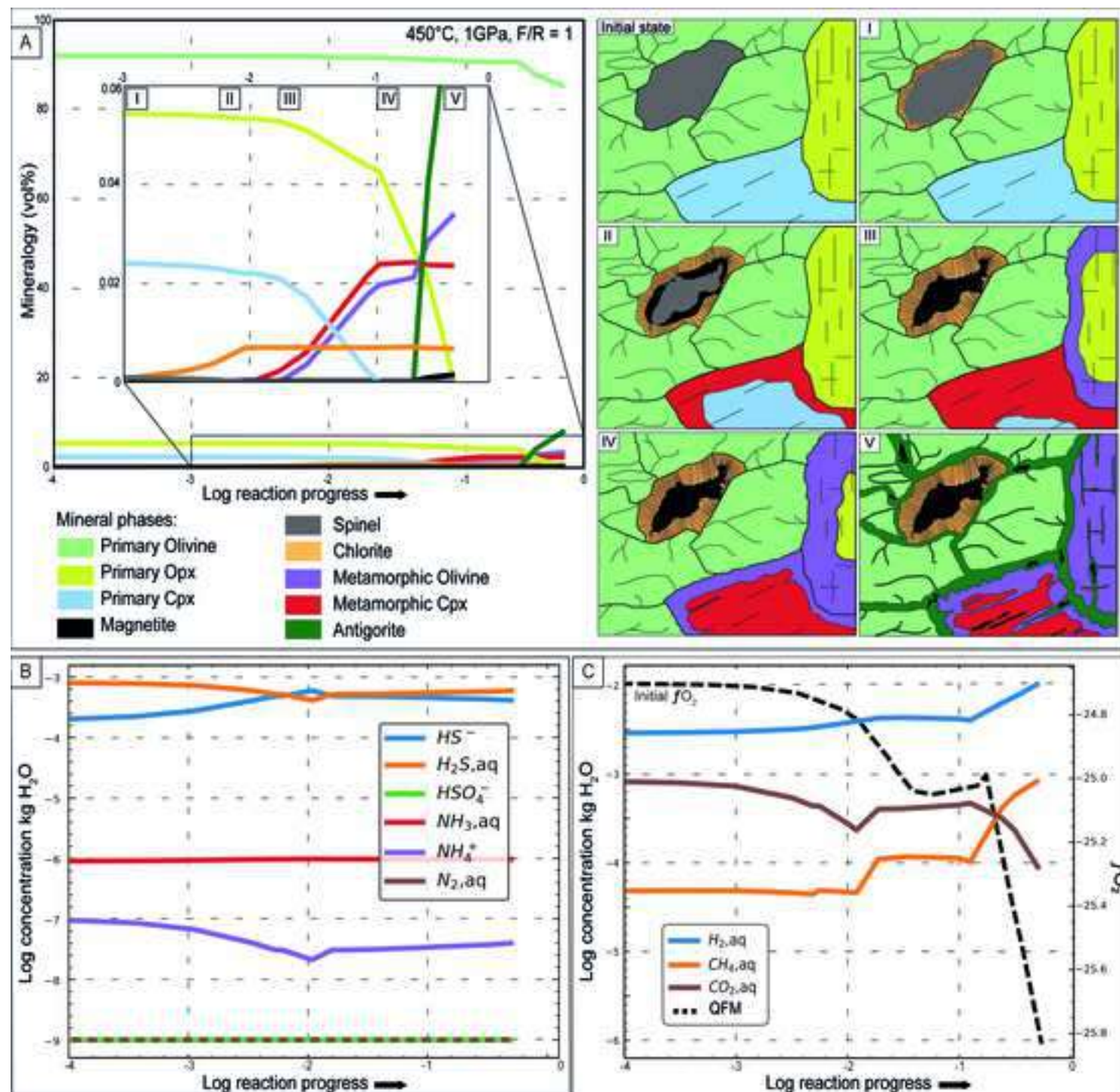


Figure 10



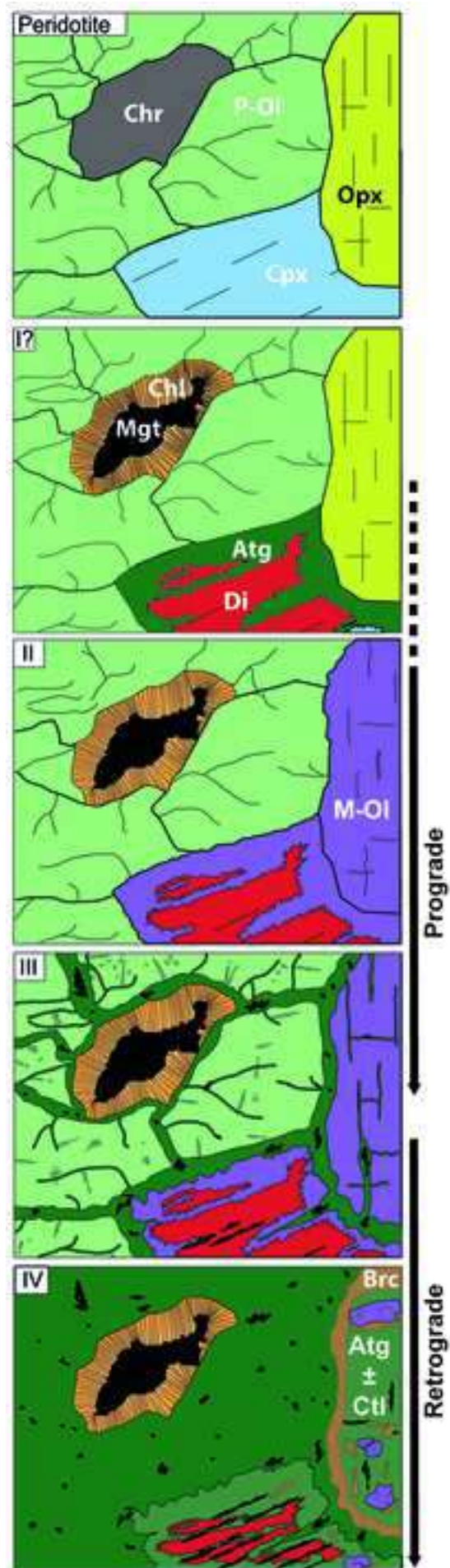
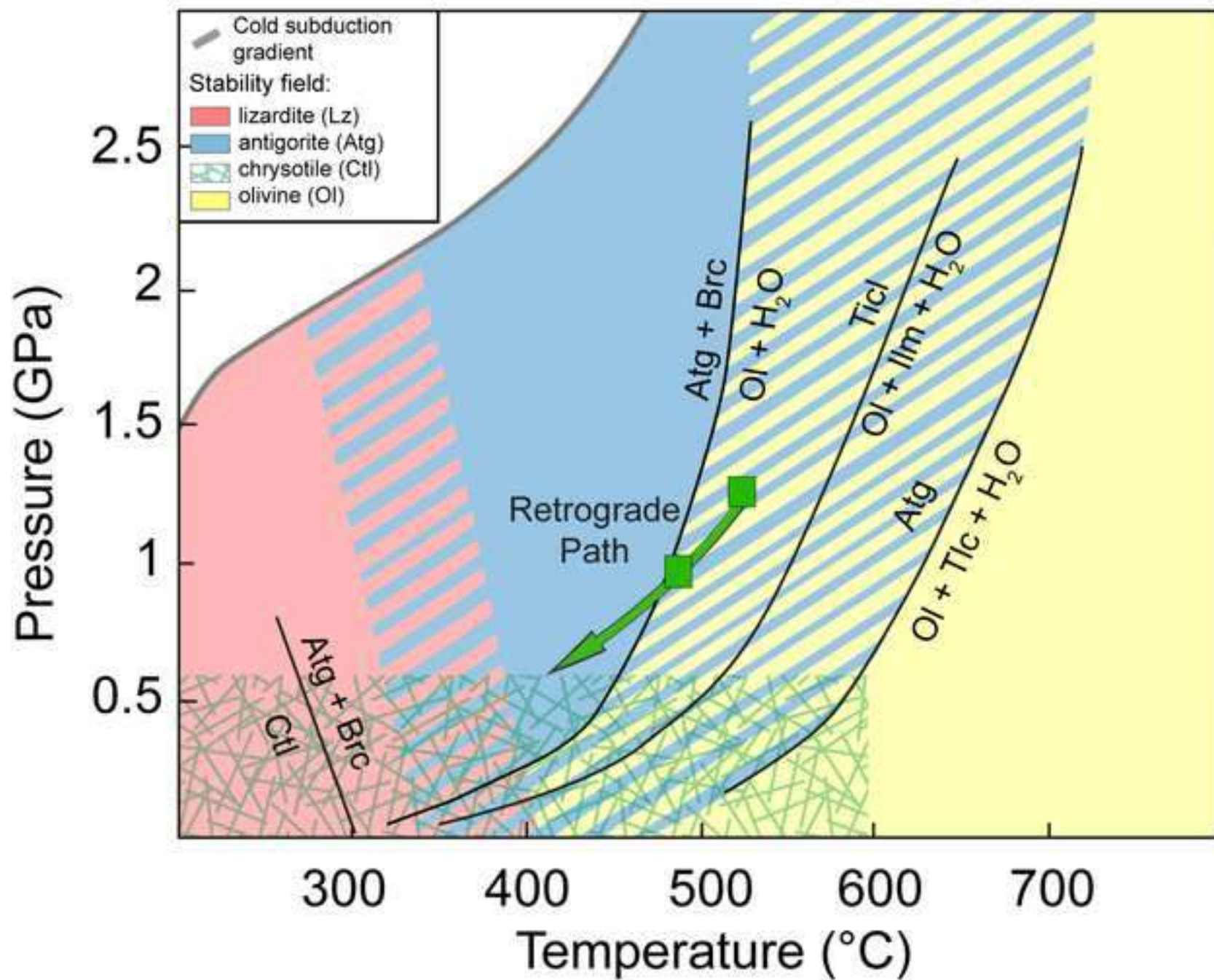


Figure 12



1 **Table 1**

MicroProbe analysis. Absence of SD value when n>1 indicates SD<0.01. *EDS analyses normalized at 100.

Minerals	Primary Olivine		Metamorphic Olivine			Pyroxene	Serpentine (Bright core)		Serpentine (Matrix)		Chlorite	
Sample	V18-2b	V18-3a	V18-2b	V18-3a	V18-B3*	V18-3a	V18-2b	V18-3a	V18-2b	V18-3a	V18-2b	V18-3a
(n)	14	11	28	15	25	20	6	2	9	4	11	1
SiO ₂	40.91 (0.25)	40.83 (0.46)	41.31 (0.49)	41.95 (0.63)	42.00 (0.12)	54.96 (0.98)	42.87 (1.21)	43.41 (0.1)	44.15 (0.17)	43.1 (1.35)	32.61 (1.34)	32.03
TiO ₂	0.01 (0.01)	0.02 (0.02)	0.02 (0.01)	0.02 (0.02)		0.03 (0.02)	0.01 (0.01)	0.02 (0.01)	0.02 (0.01)	0 (0)	0.02 (0.02)	0.00
Al ₂ O ₃	0.01 (0.01)	0.01 (0.01)	0.01 (0.02)	0.04 (0.09)		0.15 (0.11)	1.77 (1.22)	1.45 (0.78)	0.52 (0.21)	0.47 (0.26)	14.34 (2.39)	11.78
Cr ₂ O ₃	0.01 (0.02)	0.01 (0.02)	0.06 (0.18)	0.04 (0.03)		0.17 (0.11)	0.61 (0.85)	0.25 (0.19)	0.13 (0.09)	0.1 (0.1)	1.07 (0.56)	4.07
FeO (tot)	8.97 (0.34)	7.93 (0.22)	4.83 (0.30)	5.05 (0.57)	4.71 (0.19)	0.76 (0.16)	2.60 (0.26)	1.58 (0.27)	1.35 (0.22)	1.2 (0.29)	3.31 (0.46)	2.79
MnO	0.15 (0.04)	0.12 (0.06)	0.45 (0.08)	0.37 (0.06)	1.02 (0.18)	0.05 (0.03)	0.04 (0.02)	0.05 (0.05)	0.04 (0.02)	0.02 (0.02)	0.06 (0.10)	0.07
NiO	0.38 (0.03)	0.49 (0.06)	0.43 (0.07)	0.39 (0.06)	0.46 (0.08)	0.03 (0.03)	0.16 (0.02)	0.18 (0.06)	0.15 (0.04)	0.19 (0.02)	0.22 (0.05)	0.24
ZnO	0.04 (0.04)	0.03 (0.04)	0.03 (0.04)	0.03 (0.04)		0.01 (0.02)					0.02 (0.04)	0.00
MgO	50.23 (0.22)	50.91 (0.22)	52.8 (0.64)	51.8 (1.57)	51.80 (0.28)	18.75 (1.15)	37.97 (1.30)	39.81 (0.59)	39.6 (0.77)	40.07 (0.61)	34.34 (1.11)	35.08
CaO	0.02 (0.01)	0.01 (0.02)	0.02 (0.02)	0.25 (0.37)		24.87 (1.43)	0.02 (0.02)	0.05 (0.04)	0.02 (0.02)	0.02 (0.01)	0.02 (0.01)	0.05
Na ₂ O	0.09 (0.22)	0.01 (0.01)	0.02 (0.02)	0.01 (0.01)		0.04 (0.02)					0.02 (0.03)	0.03
K ₂ O	0.01 (0.02)	0.01 (0.01)	0.01 (0.01)	0.01 (0.01)		0.01 (0.01)					0.02 (0.02)	0.02
Total,	100.82 (0.36)	100.37 (0.70)	100.06 (1.10)	99.96 (1.63)	100	99.83 (1.12)	86.2 (0.63)	86.93 (0.4)	86.07 (0.82)	85.25 (1.66)	86.14 (0.65)	86.17
Cations												
Si	0.990	0.988	0.991	1.012	1.013	1.989	1.984	2.010	2.044	1.995	6.232	6.165
Ti	0.000	0.000	0.000	0.000		0.001	0.000	0.001	0.001	0.000	0.004	0.000
Al	0.000	0.000	0.000	0.001		0.006	0.091	0.079	0.028	0.026	3.229	2.672
Cr	0.000	0.000	0.001	0.001		0.005	0.026	0.009	0.005	0.004	0.162	0.619
Fe ²⁺ (tot)	0.181	0.161	0.097	0.102	0.095	0.023	0.104	0.061	0.052	0.046	0.529	0.404
Mn	0.003	0.003	0.009	0.008	0.021	0.002	0.001	0.002	0.002	0.001	0.010	0.012
Ni	0.007	0.010	0.008	0.008	0.009	0.001	0.006	0.007	0.006	0.007	0.034	0.037
Zn	0.001	0.001	0.000	0.001		0.000					0.003	0.000
Mg	1.812	1.837	1.891	1.861	1.862	1.012	2.486	2.747	2.733	2.765	9.782	10.063
Ca	0.000	0.000	0.001	0.006		0.964	0.001	0.002	0.001	0.001	0.003	0.011
Na	0.004	0.000	0.001	0.000		0.003					0.007	0.012
K	0.000	0.000	0.000	0.000		0.000					0.005	0.005
Mg#	0.91	0.92	0.95	0.95	0.95	0.98	0.94	0.96	0.97	0.97	0.95	0.96

Mg# = Mg/(Mg+ΣFe)

3 **Table 2**

MicroProbe analysis. Absence of SD value when n>1 indicates SD<0.01

Minerals	Spinel (nucleus)	Spinel (intermediate)	Magnetite (rim)	Magnetite (mesh and veins)	Brucite
Sample	V18-3a	V18-3a	V18-3a	V18-3a	V18-2b
(n)	7	7	7	1	10
SiO ₂	0.02 (0.02)	0.03 (0.01)	0.06 (0.07)	0.07	0.05 (0.03)
TiO ₂	0.09 (0.02)	0.23 (0.05)	0.03 (0.02)	0.04	0.01 (0.01)
Al ₂ O ₃	12.63 (0.94)	3.87 (1.34)	0.00	0.03	0.01 (0.01)
Cr ₂ O ₃	47.51 (0.57)	41.6 (1.29)	1.87 (1.16)	0.01	0.02 (0.02)
FeO	34.12 (1.1)	48.32 (2.02)	91.45 (0.75)	92.44	92.57 (0.28)
MnO	0.34 (0.04)	0.95 (0.36)	0.16 (0.03)	0.12	0.19 (0.05)
NiO	0.09 (0.02)	0.27 (0.05)	1.05 (0.1)	1.11	0.82 (0.09)
ZnO	0.49 (0.08)	0.3 (0.1)	0.04 (0.06)	0.10	0.04 (0.08)
MgO	5.99 (0.32)	3.37 (0.22)	0.71 (0.09)	0.62	0.82 (0.19)
CaO	0.01 (0.01)	0.00	0 (0.01)	0.00	0.00
Na ₂ O	0.03 (0.04)	0.02 (0.02)	0.03 (0.03)	0.03	0.02 (0.04)
K ₂ O	0.00	0.01 (0.01)	0 (0.01)	0.01	0.00
Total	101.4 (0.56)	99.03 (0.6)	95.46 (0.5)	94.63	94.56 (0.45)
Cr#	0.79(0.01)	0.92(0.2)	1.00		

4 Cr# = Cr/(Al+Cr)

5 **Table 3**

MicroProbe analysis of alloys

Sample	V18-2b						V18-3a		
Alloy	NiFeCu	NiS	NiS	NiS	NiFeCu	NiFeCu	NiS	NiS	NiS
S		24.06	24.25	24.12			24.59	24.52	24.50
Fe	12.21	0.9	0.51	1.35	13.35	20.07	0.84		0.95
Pb				0.13			0.18		
Ni	86.23	72.68	72.71	73.55	86.05	80.03	72.97	72.85	73.30
Cu	1.94				1.75	1.49			
Total:	100.45	97.9	97.59	99.18	101.28	101.71	98.70	97.72	99.04

6 **Table 4**

Calculated partition coefficient between antigorite and olivine for Mg and Mn

Calculated K _D	K _D Mg		K _D Mn	
	V18-2	V18-3b	V18-2	V18-3b
Atg1 / P-OI	0.25	0.14	0.42	0.54
Atg2 / P-OI	0.11	0.11	0.42	0.27
Atg1 / M-OI	0.49	0.23	0.14	0.18
Atg2 / M-OI	0.21	0.17	0.14	0.09

K_D Atg/OI from bibliography

0.45-0.35

0.18

K_D Atg/OI Mg from Evans et al.(2008) and Mn from Trommsdorff and Evans, 1974.